Prepared for submission to JHEP

Bootstrapping $\mathcal{N} = 4$ sYM correlators using integrability

Simon Caron-Huot[1], **Frank Coronado**[1], **Anh-Khoi Trinh**[1], **Zahra Zahraee**[1]

[1] *Department of Physics, McGill University, 3600 Rue University, Montréal, H3A 2T8, QC Canada*

E-mail: schuot@physics.mcgill.ca, fcidrogo@gmail.com, anh-khoi.trinh@mail.mcgill.ca, zr.zahraee@physics.mcgill.ca

Abstract: How much spectral information is needed to determine the correlation functions of a conformal theory? We study this question in the context of planar supersymmetric Yang-Mills theory, where integrability techniques accurately determine the single-trace spectrum at finite 't Hooft coupling. Corresponding OPE coefficients are constrained by dispersive sum rules, which implement crossing symmetry. Focusing on correlators of four stress-tensor multiplets, we construct combinations of sum rules which determine one-loop correlators, and we study a numerical bootstrap problem that nonperturbatively bounds planar OPE coefficients. We observe interesting cusps at the location of physical operators, and we obtain a nontrivial upper bound on the OPE coefficient of the Konishi operator outside the perturbative regime.

Contents

1 Introduction **2**

2 Setup and methods **4**
- 2.1 Stress tensor multiplet correlators 4
- 2.2 Decoupling double-traces 6
- 2.3 Input from integrability: Spectrum from quantum spectral curve 8
- 2.4 Properties of the Konishi operator at weak and strong coupling 14

3 A menu of functionals **16**
- 3.1 Dispersion relations in Mellin space 17
- 3.2 Projection functionals derived from B_v 19
- 3.3 Convergence of Mellin functionals 21
- 3.4 List of functionals we used 23

4 Numerical bootstrap **23**
- 4.1 Generalities 24
- 4.2 Bounds at weak coupling: toy problem with 2 functionals 26
- 4.3 Bounds at weak coupling: adding more functionals 26
- 4.4 Stronger coupling: $g = 0.3$ 30

5 Discussion **32**

A Additional formulas from integrability **33**

B Projection Functionals **35**
- B.1 Action of $\widehat{B}_{\mathrm{t}}$ on operators near twist two 35
- B.2 One-loop anomalous dimensions: the $\Phi_{\ell,\ell+2}$ projection functionals 37
- B.3 One-loop OPE coefficients: the Ψ_ℓ functionals 39
- B.4 Formulas for evaluating Φ and Ψ functionals 40
- B.5 Sign properties of Φ and Ψ functionals 41

C Formulas for efficient evaluation of functionals **42**
- C.1 Dispersion relations in position space 42
- C.2 Mack polynomials 45
- C.3 Formulas for B functionals using Mack polynomials 46
- C.4 Formulas for Polyakov-Regge blocks using Mack polynomials 48
- C.5 Some algorithmic improvements 50

1 Introduction

The study of $\mathcal{N} = 4$ supersymmetric Yang-Mills theory (sYM) has driven advancements in key areas of theoretical physics, including insights into the AdS/CFT correspondence through the development of scattering amplitudes, correlation functions, supersymmetric localization, integrability, and the conformal bootstrap. Some of these techniques offer exact results in special subsectors, while others are perturbative approximations which often exploit exact results as boundary conditions. It is interesting to ask to what extent the full theory is nonperturbatively determined by exact subsectors.

In the planar 't Hooft limit $\mathcal{N} = 4$ sYM, integrability has led to impressive advancements for the computation of the spectrum of local operators, some correlations functions and scattering amplitudes at finite coupling in various kinematical limits [1–3]. This boundary data was instrumental in recent perturbative scattering amplitudes and form factors which reached a record high loop order (8 loops) [4] and high multiplicity (up to seven-points) [5, 6]. In the strong coupling limit, most efforts have focused on correlators of $\frac{1}{2}$-BPS operators, which is primarily driven by string theory, supergravity, conformal bootstrap, and supersymmetric localization [7, 8] techniques. Stringy corrections [9–11] and non-planar corrections [12, 13] have been computed for four points, while the highest multiplicity correlator is the tree-level five-point function [14], obtained by exploiting all existing constraints. Although still out of reach for most observables, these developments suggest that more quantities will eventually be computed at finite coupling in this theory.

A promising nonperturbative avenue originates from the integrability literature: in the planar limit, the spectral problem is completely solved as a result of the Quantum Spectral Curve (QSC) [15–17], which governs the spectrum of single-trace operators at arbitrary values of the coupling; see ref. [18] for a recent pedagogical review. At the moment the QSC only provides spectrum of single-trace operators, and therefore dynamics, encoded through OPE coefficients for example, remain elusive at finite coupling. Nonetheless, there are encouraging developments with respect to the hexagon [19–22] and octagon [23, 24] formalisms, which may overcome this challenge; the hexagon and octagon formalisms reinterpret the Feynman expansion as the scattering of magnons and they are readily computable in the large R-charge limit. Unfortunately, away from this limit, the complexity of such computations grow exponentially.

An independent nonperturbative framework is the numerical conformal bootstrap [25–27]. The latter combines unitarity, crossing symmetry, and other nonperturbative constraints to resolve the spectrum of a generic conformal field theory and to bound its OPE coefficients; see [28] for a recent review of numerical bootstrap results. In the context of $\mathcal{N} = 4$ sYM, this method provides a handle into energy-momentum correlation functions for finite gauge groups $\mathrm{SU}(N_c)$ [29], and, when combined with exact results from localization, arbitrary 't Hooft coupling [8].

It was recently proposed that integrability and bootstrap techniques could be combined to solve $\mathcal{N} = 4$ sYM in the planar limit [30, 31]. The authors introduced an approach

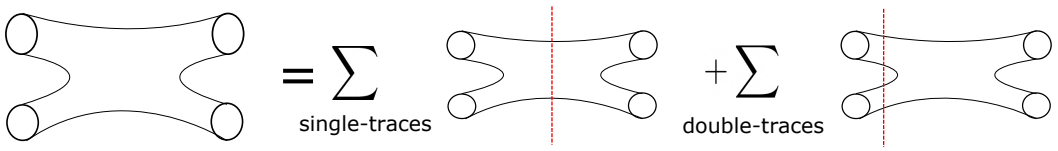

Figure 1: A connected correlator in the planar limit: its operator product expansion receives contributions from single and double trace operators. The latter's OPE data scale at large-N_c like $\lambda_{\mathcal{O}\mathcal{O}[\mathcal{O}\mathcal{O}]} \sim 1 + O(1/N_c^2)$, where the "1" yields the disconnected correlator and the $O(1/N_c^2)$ corrections enter the figure.

("Bootstrability") to study the 1D defect CFT defined by inserting local operators along a $\frac{1}{2}$-BPS Wilson line in $\mathcal{N} = 4$ sYM. Taking exact spectral data as input from integrability, they used bootstrap techniques to derive tight bounds on the OPE coefficients of the first few lightest operator in the spectrum.

In this paper, we tackle a similar problem for a fully four-dimensional correlator involving four stress tensors in the planar limit of $\mathcal{N} = 4$ sYM theory, meaning the $N_c \to \infty$ of a SU(N_c) gauge theory with fixed 't Hooft coupling $\lambda = g_{\text{YM}}^2 N_c$. We will use spectral information from integrability, together with suitable nonperturbative sum rules on the spectrum, to constrain OPE coefficients. In the planar limit, both single-trace and double-trace operators are exchanged as illustrated in fig. 1. The spectrum of single-trace operators can be calculated precisely owing to the QSC. Our goal will be to use the numerical bootstrap to bound the OPE coefficient of the lightest unprotected single-trace operators in the spectrum, the so-called Konishi operator.

At strong coupling, the Konishi operator is dual to a genuine massive string mode. Its properties have been studied extensively over the years. Its scaling dimension has been computed perturbatively in both weak and strong 't Hooft coupling limits [32, 33], results which are now exactly connected at intermediate coupling by the QSC [15, 34, 35]. However, less is known about the Konishi operator's OPE coefficient. It has been computed up to five loops in the weak coupling limit [36], and is known to the leading order at strong coupling through its connection with the flat-space Veneziano-Shapiro amplitude [9, 10, 37]. Can it be bootstrapped at finite coupling, given spectral information from the QSC?

While our work is similar in spirit to refs. [30, 31], the passage from $D = 1$ defects to $D = 4$ correlators presents significant challenges. A main one is that an infinite number of double-trace operators enter the OPE, polluting it with undesirable operators about which we have no spectral information. Worse, the numerical bootstrap leverages the positivity of OPE coefficients, but $O(1/N_c^2)$ corrections to OPE coefficients control planar correlators (see fig. 1) and do not have definite signs. These hurdles are overcome by the recently introduced dispersive CFT functionals [38–41], which decouple the double-traces; planar correlators are reconstructed from single-trace data only [42]. This work constitutes the first systematic

application of dispersive functionals to a numerical bootstrap problem. A second challenge is that the single-trace operators entering the OPE are more numerous than in 1D, being now labelled by dimension and spin, but in practice only a finite number of dimensions can be computed from the QSC.

This paper is organized as follows. In section 2, we describe our setup by detailing properties of the stress tensor multiplet correlator, the decoupling of the double-twist sector, and aspects of integrability relevant for our bootstrap algorithm. In section 3, we discuss the dispersive functionals used in this paper; details of their construction and numerical evaluation are described in the appendix. Section 4 contains our primary results – bounds on the OPE coefficient of the Konishi operator – obtained from the numerical bootstrap. Finally, we summarize our findings and discuss future work in section 5. Three appendices review integrability formulas; detail our construction of functionals which solve the 1-loop problem; and detail efficient formulas for numerically evaluating of dispersive functional.

2 Setup and methods

2.1 Stress tensor multiplet correlators

We consider the simplest half-BPS operator in the sYM theory, which transforms as a symmetric traceless tensor $\mathrm{so}(6)_R$. Its supermultiplet notably contains the stress tensor. Working in index-free notation, this operator can be viewed as function of spacetime coordinates x and a null 6-vector y:

$$\mathcal{O}(x,y) \propto \mathrm{Tr}\left[(y\cdot\phi(x))^2\right] . \tag{2.1}$$

We use the canonical normalization $\langle\mathcal{O}(x_1,y_1)\mathcal{O}(x_2,y_2)\rangle = (y_{12}^2/x_{12}^2)^2$. Due to conformal symmetry, the four-point correlator factors through spacetime and R-charge cross-ratios,

$$u = \frac{x_{12}^2x_{34}^2}{x_{13}^2x_{24}^2} = z\bar{z}\,, \qquad v = \frac{x_{23}^2x_{14}^2}{x_{13}^2x_{24}^2} = (1-z)(1-\bar{z})\,, \tag{2.2}$$

$$\sigma = \frac{y_{12}^2y_{34}^2}{y_{13}^2y_{24}^2} = \alpha\bar{\alpha}\,, \qquad \tau = \frac{y_{23}^2y_{14}^2}{y_{13}^2y_{24}^2} = (1-\alpha)(1-\bar{\alpha})\,. \tag{2.3}$$

Furthermore, superconformal Ward identities constrain the dependence on R-charge vectors. Namely, they imply that the correlator with $z=\alpha$ is protected and does not depend on the coupling. This allows to separate the free theory limit ($g^2\to 0$) from the dynamical part $\mathcal{H}$ of the correlator [43, 44]:

$$\begin{aligned}\frac{x_{13}^4x_{24}^4}{y_{13}^4y_{24}^4}\langle\mathcal{O}(x_1,y_1)\cdots\mathcal{O}(x_4,y_4)\rangle &= 1+\frac{\sigma^2}{u^2}+\frac{\tau^2}{v^2}+\frac{1}{c}\left(\frac{\sigma}{u}+\frac{\tau}{v}+\frac{\sigma\tau}{uv}\right)\\ &\quad+\frac{1}{c}(z-\alpha)(z-\overline{\alpha})(\overline{z}-\alpha)(\overline{z}-\overline{\alpha})\mathcal{H}(z,\overline{z})\,,\end{aligned} \tag{2.4}$$

where $c\equiv\frac{N_c^2-1}{4}$, and $\mathcal{H}$ is independent of R-symmetry cross-ratios $\alpha,\overline{\alpha}$, which only appear in its prefactor. We are interested in the planar limit, where $\mathcal{H}$ is N_c-independent.

The function $\mathcal{H}$ effectively behaves like a correlator of four scalar primaries with $\Delta = 4$. It enjoys the following properties:

1. Crossing:
$$\mathcal{H}(u,v) = \mathcal{H}(v,u) = u^{-4}\mathcal{H}(\tfrac{1}{u}, \tfrac{v}{u}). \tag{2.5}$$

2. Operator Product Expansion: it can be expressed as a sum of short (protected) and long (unprotected) multiplets, the latter being labelled by their dimension and spin (Δ, J):
$$\mathcal{H}(u,v) = \mathcal{H}^{\text{protected}}(u,v) + \sum_{(\Delta,J)\ \text{long}} \lambda^2_{\Delta,J} G^{N=4}_{\Delta,J}(u,v), \qquad G^{N=4}_{\Delta,J} \equiv u^{-4} G_{\Delta+4,J}\,. \tag{2.6}$$
The protected part, equal to minus the $g \to 0$ limit of the sum, will be discussed below.

3. Regge limit: as $z, \overline{z} \to \infty$ with fixed ratio $z/\overline{z}$, $\mathcal{H} \sim z^{J_*-4}$ where z is the Regge intercept. Nonperturbatively in N_c we have $J_* \leq 1$, ie. the quantity $uv\mathcal{H}$ is bounded. In the planar limit this bound becomes trivial because of the overall $1/c$, but the bound of chaos still ensures $J_* \leq 2$, which is saturated at infinite 't Hooft coupling. We will assume that at finite coupling, $J_* < 2$ strictly.

4. Weak and Strong limits: in our conventions, at extreme values of the 't Hooft coupling ($g^2 \equiv \frac{g^2_{\text{YM}} N_c}{16\pi^2}$) [45],
$$\begin{aligned} &\lim_{g^2\to 0} \mathcal{H}(u,v) = -2g^2 \frac{F_1(u,v)}{uv} + O(g^4)\,, \\ &\lim_{g^2\to \infty} \mathcal{H}(u,v) = \mathcal{H}^{\text{strong}}(u,v) + O(1/g) \quad \text{with} \quad \mathcal{H}^{\text{strong}} = -\bar{D}_{2,4,2,2}\,. \end{aligned} \tag{2.7}$$

In the above, we use the standard conformal block
$$G_{\Delta,J}(u,v) = \frac{z\overline{z}}{\overline{z}-z}\left[k_{\frac{\Delta-J-2}{2}}(z) k_{\frac{\Delta+J}{2}}(\overline{z}) - k_{\frac{\Delta+J}{2}}(z) k_{\frac{\Delta-J-2}{2}}(\overline{z})\right] \tag{2.8}$$
with $k_h(z) = z^h {}_2F_1(h,h,2h,z)$. Furthermore, F_1 is the box integral and $\bar{D}_{2,4,2,2}$ is a derivative of it (see [46]):
$$F_1(u,v) \equiv \frac{2\text{Li}_2(z) - 2\text{Li}_2(\overline{z}) + \log(z\overline{z})(\log(1-z) - \log(1-\overline{z}))}{z-\overline{z}}\,, \tag{2.9}$$
$$\bar{D}_{2,4,2,2} = \partial_u \partial_v (1 + u\partial_u + v\partial_v) F_1(u,v)\,. \tag{2.10}$$

Note that we have factored the large-N_c scaling of the single-trace OPE coefficients into λ^2 so that λ does not depend on N_c:
$$\lambda^2_{\Delta,J}\Big|_{\text{canonical}} = \frac{1}{c}\lambda^2_{\Delta,J}. \tag{2.11}$$
As an abuse of notation we will still refer to λ as OPE coefficients.

In the planar limit $c \to \infty$, the OPE (2.6) receives contributions only from single- and double-trace operators. Our main goal will be to constrain the single-trace coefficients $\lambda^2_{\Delta,J}$ given input about the single-trace spectrum from integrability.

2.2 Decoupling double-traces

For our purposes, the double-trace contribution to the OPE is a nuisance. Since double-traces enter already in the disconnected correlator ($\sim c^0$ terms in eq. (2.4)), their contributions to $\mathcal{H}$ represent $1/c$ corrections to coefficients and scaling dimensions that do not have definite signs. To formulate a nonperturbative bootstrap in the planar limit, it is crucial to project out all double-traces.

This is naturally achieved by taking a double-discontinuity of the correlator. For $z, \overline{z} < 0$, let:

$$\text{dDisc}_s \mathcal{H}(z,\overline{z}) \equiv \mathcal{H}(z_{\curvearrowleft}, \overline{z}_{\curvearrowright}) - \tfrac{1}{2}\mathcal{H}(z_{\curvearrowleft}, \overline{z}_{\curvearrowleft}) - \tfrac{1}{2}\mathcal{H}(z_{\curvearrowright}, \overline{z}_{\curvearrowright}) \,, \tag{2.12}$$

where the arrows denote analytic continuation paths starting from the Euclidean region with $0 < z, \overline{z} < 1$. The first term is simply the Euclidean correlator (the path maintains $\overline{z} = z^*$), which enjoys the usual OPE, while for the other terms the analytic continuation simply adds phases, so the OPE (2.6) yields

$$\text{dDisc}_s \mathcal{H}(z,\overline{z}) = \text{dDisc}_s \mathcal{H}^{\text{protected}}(z,\overline{z}) + \sum_{(\Delta,J)\ \text{long}} 2\sin^2\left(\pi \tfrac{\Delta - J}{2}\right) \lambda^2_{\Delta,J} G^{N=4}_{\Delta,J}(z,\overline{z}) \,. \tag{2.13}$$

The crucial point is the trigonometric factor, which has double-zeroes at the position of double trace operators, $\Delta - J = 4 + 2m + O(1/c)$ with $m \in \mathbb{N}$. Thus, in the planar limit, the above sum is saturated by single-trace operators.

The protected double-discontinuity is simple to describe: only operators of twist exactly two, from the stress-tensor multiplet, contribute. Taking the singular terms in eq. (2.31) of [29], we find

$$\text{dDisc}_s \mathcal{H}^{\text{protected}}(u,v) = f^{(0)}(v) \text{dDisc}_s \frac{1}{u} \quad \text{with} \quad f^{(0)}(v) \equiv \frac{v^2 - 1 - 2v\log v}{v(1-v)^3} \,. \tag{2.14}$$

Note that the double-discontinuity of $1/u$ is a nonvanishing singular distribution near $u = 0$ [47]. A simple check is that this is precisely the double-discontinuity of the strong coupling result (2.7):

$$\lim_{u\to 0} \mathcal{H}^{\text{strong}}(u,v) = \frac{f^{(0)}(v)}{u} + (\text{terms with vanishing dDisc}_s). \tag{2.15}$$

This happens because in the supergravity limit all non-protected single-traces become heavy and decouple from (2.13).

The double-discontinuity kills double-traces but is not crossing symmetric since it picks a specific channel (above, the s-channel). How do we get crossing equations? The nontrivial fact is that conformal correlators are uniquely determined by their double-discontinuity and Regge limits. Concretely, they can be reconstructed through dispersive integrals [42]:

$$\mathcal{H}(u,v) = \int_s du' dv' K(u,v;u',v') \ \text{dDisc}[\mathcal{H}(u',v')] \,. \tag{2.16}$$

The kernel K is recorded in eq. (C.1) but won't be important for the present discussion. The integration region lies inside s-channel kinematics $z', \bar{z}' \leq 0$, where the OPE (2.13) converges. (The integration region is further restricted by step-functions and delta-functions inside K.) By defining "Polyakov-Regge block" as the dispersive transform of a single s-channel block,

$$\mathcal{P}^{N=4}_{u,v}[\Delta, J] \equiv \int_s du'dv' K(u,v;u',v') \ \mathrm{dDisc}_s[G^{N=4}_{\Delta,J}(u',v')]\,, \tag{2.17}$$

the correlator can thus be expressed as

$$\mathcal{H}(u,v) = \mathcal{H}^{\text{strong}}(u,v) + \sum_{(\Delta,J)\ \text{long}} \lambda^2_{\Delta,J} \mathcal{P}^{N=4}_{u,v}[\Delta, J]. \tag{2.18}$$

The crucial point is that only *single-traces* enter this sum in the planar limit, since $\mathcal{P}$ inherits the double zeroes from dDisc. The protected contribution is simply $\mathcal{H}^{\text{strong}}(u,v)$ because of the decoupling just mentioned; we verified this numerically from the formulas in appendix.

The above is valid for any Euclidean u, v, namely, u and v which come from complex-conjugate cross-ratios $\bar{z} = z^*$. This condition can be stated as:

$$\text{Euclidean region: } u, v > 0 \text{ real} \quad \text{and} \quad 4uv \geq (1-u-v)^2. \tag{2.19}$$

The dispersive representation manifests $u \leftrightarrow v$ crossing symmetry, which correspond to the $s \leftrightarrow t$-channel crossing equation: $\mathcal{P}^{N=4}_{\Delta,J}(u,v) = \mathcal{P}^{N=4}_{\Delta,J}(v,u)$. To get crossing relations, the idea is that the second relation in (2.5) is nontrivial, and amounts to an infinite number of constraints:

$$\boxed{0 = \sum_{(\Delta,J)\ \text{long}} \lambda^2_{\Delta,J} X_{u,v}[\Delta, J] \quad \text{with} \quad X_{u,v} \equiv \mathcal{P}_{u,v} - u^{-4}\mathcal{P}_{1/u,v/u}\,, \quad \text{for } (u,v) \text{ Euclidean.}} \tag{2.20}$$

This statement of crossing symmetry involves only single-trace data in the planar limit.

It is not the most general statement yet, because the (unsubtracted) dispersion relation (2.16) only relied on the Regge behavior $J_* < 4$. (The threshold is shifted by four compared with the usual threshold of an unsubtracted dispersion relation due to supersymmetry and the factors in (2.4).) But since we expect $J_* < 2$ at finite 't Hooft coupling, more is true: *anti-subtracted* dispersion relations converge. As explained in [39] and reviewed in section 3.1, the difference between different subtraction schemes are "dispersive sum rules" characterized by their patterns of zeroes on double-twist operators. Here we are not allowed to cancel any double-trace zero, so there is only a one-parameter family of extra constraints. We can take it to be the $B_{2,v}$ sum rule in eq. (4.39) of [39] applied to $u'v'\mathcal{H}$. Dividing it by v, we will call it simply the B_v functional:

$$B_v[f(u',v')] = \int_v^\infty dv' \int_0^{(\sqrt{v'}-\sqrt{v})^2} du' \frac{v'-u'}{\pi^2 v\sqrt{v^2 - 2(u'+v')v + (u'-v')^2}} \mathrm{dDisc}_s[f(u',v')]. \tag{2.21}$$

It can be proved directly that $B_v[\mathcal{H}] = 0$, essentially by deforming the integration contour from the s-channel to the t-channel double-discontinuity, and exploiting $u' \leftrightarrow v'$ antisymmetry of the integrand [39]. For a generic correlator the contour deformation would pick a contribution from u-channel identity, but this is absent for $\mathcal{H}$. The integral against $(u')^\delta$ becomes singular for $u' \to 0$ if $\delta \leq -1$, but can be defined by analytic continuation in δ. One finds in this way that when acting on twist-two exchanges, B_v simply returns the coefficient of $1/u$ [39], so $B_v[\mathcal{H}^{\text{protected}}]$ gives

$$B_v^{\text{protected}} = f^{(0)}(v) \tag{2.22}$$

with $f^{(0)}(v)$ in (2.14). Therefore, the B_v sum rules take the form:

$$\boxed{0 = B_v^{\text{protected}} + \sum_{(\Delta,J)\ \text{long}} \lambda^2_{\Delta,J} B_v[\Delta, J] \qquad (v > 0 \text{ real}).} \tag{2.23}$$

Here and below we use the notation $B_v[\Delta, J] \equiv B_v[G^{N=4}_{\Delta,J}]$ for the action of a functional on a block. The salient feature of these sum rules is the protected contribution, which will provide an absolute normalization to OPE coefficients; it will play a similar role in our analysis as the identity operator in numerical bootstrap studies. At strong coupling, it can be interpreted as a relation between protected graviton exchanges and heavy string modes. It is crucial for its validity that the 't Hooft coupling is finite, so the Regge intercept is strictly less than 2.

The crossing relation (2.20) and B_v sum rule (2.21) will be our main tool: they exhaust the constraints on single-trace data coming from crossing symmetry and good Regge behavior. Formulas for their efficient numerical evaluation are detailed in appendix C. Following the bootstrap method, the key idea will be to exploit positivity of the unknowns $\lambda^2_{\Delta,J}$.

2.3 Input from integrability: Spectrum from quantum spectral curve

Operators in $\mathcal{N} = 4$ SYM can be identified through their charges under the global symmetries, the conformal group $SO(4,2)$: $\{\Delta, J_1, J_2\}$ and the R-symmetry group $SO(6)$: $\{r_1, r_2, r_3\}$. However, the real "fingerprint" of a (single-trace) operator is its set of charges under the infinite family of symmetries that make the theory integrable. This fingerprint is encoded in a QSC [16, 34]. The latter is composed of a set of 8 functions: $P_a(u)$ and $Q_j(u)$ with indices $a, j \in \{1, 2, 3, 4\}$, which depend on the spectral parameter u.[1] For each operator, there is a unique set $\{P_a, Q_j\}$. In particular, the global charges are recovered in their large-u asymptotics:

$$P_a(u) \underset{u\to\infty}{\sim} u^{M_a} \qquad \text{and} \qquad Q_j(u) \underset{u\to\infty}{\sim} u^{\hat{M}_j}. \tag{2.24}$$

Since we look at a single correlation function, of the stress-tensor multiplet, all the operators we are interested in have the same R-charges, and spacetime charges of the form $(\Delta, J_1 =$

[1] We recognize the overload of the letter "u", which represents in turn the cross-ratio u, the spectral parameter u, and below, the Mellin-Mandelstam variable u. We hope that no confusion will appear from the context.

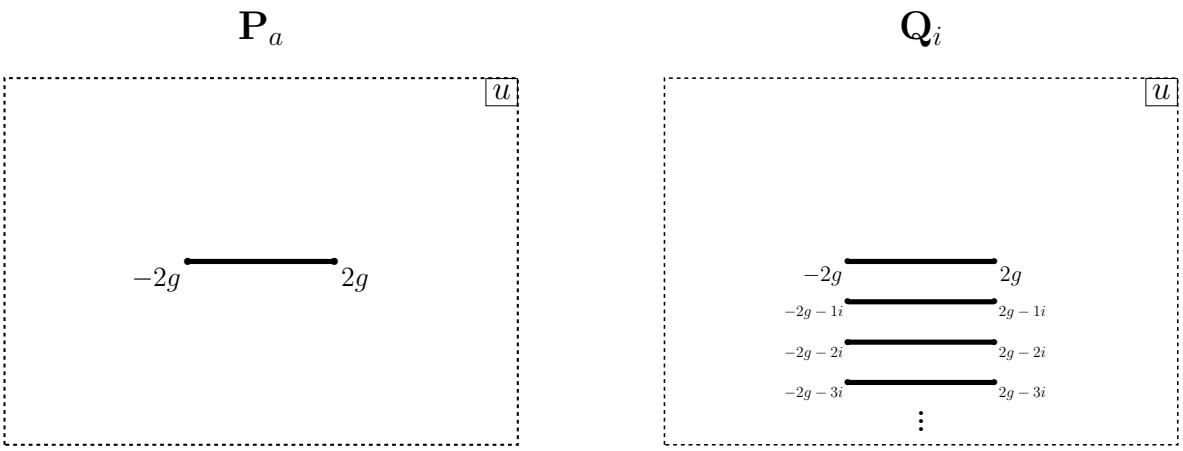

Figure 2: Analytic structure of P_a and Q_j. The P_a have a single square-root type branch cut at $u \in [-2g, 2g]$, while the Q_j have an infinite ladder of short branch cuts in the lower half-plane. Alternatively, the principal sheet of Q_j could be defined so it is an analytic function outside two long cuts on the real axis.

$J+2$, $J_2 = 0$, $r_i = 0$), corresponding to the exponents:

$$M_a = \{-2, -1, 0, 1\}, \qquad \hat{M}_j = \{\tfrac{\Delta - J}{2}, \tfrac{\Delta + J + 2}{2}, \tfrac{-\Delta - J - 4}{2}, \tfrac{-\Delta + J - 2}{2}\}. \tag{2.25}$$

In this paper we use the quantum spectral curve to determine the scaling dimensions for a few values of the coupling g for the first few primary operators in the leading and sub-leading Regge trajectories. Specifically, we consider the operators with the following identification at weak coupling:

$$\begin{aligned} \text{leading trajectory: } & \Delta = 2 + J + O(g^2) \quad \text{for} \quad J = 0, 2, 4, 6, 8, 10, \\ \text{subleading trajectory: } & \Delta = 4 + J + O(g^2) \quad \text{for} \quad J = 0\,. \end{aligned} \tag{2.26}$$

Additionally, we will use the Asymptotic Bethe Ansatz to study the leading and subleading trajectory at asymptotically large spins.

We now briefly review how the QSC is solved to find the dimension Δ of a given operator. The starting point is the analytic properties of the P_a, which is analytic outside a short cut $[-2g, 2g]$, where it has a square-root branch point, see figure 2. This allows to parametrize it as

$$P_a(u) \;=\; x^{M_a} \sum_{n=0}^{\infty} \frac{c_{a,n}}{x^{2n}}, \tag{2.27}$$

where the Zhukovsky variable is

$$x(u) = \frac{u + \sqrt{u - 2g}\sqrt{u + 2g}}{2g} \tag{2.28}$$

The series proceeds in even powers of $1/x$ due to the left-right symmetry of our operators [16]. The QSC equations allow us to gauge-fix $c_{4,1} = 0$. This parametrization converges in a

neighborhood of the cut on the second sheet, where the continued function is obtained by a simple replacement $x \mapsto 1/x$:

$$\tilde{P}_a(u) \;=\; x^{-M_a} \sum_{n=0}^{\infty} c_{a,n}\, x^{2n}\,. \tag{2.29}$$

Given $P_a(u)$, the $Q_j(u)$ are obtained by solving a finite difference equation known as P-Q system. It involves an intermediate function $Q_{a|j}(u)$ which satisfies

$$Q_{a|j}(u+i/2) - Q_{a|j}(u-i/2) = P_a(u)\, Q_j(u) \tag{2.30}$$

where

$$Q_j(u) = P_a(u) Q_{b|j}(u+i/2)\, \chi^{ab} \tag{2.31}$$

with $\chi^{ab} = (-1)^a \delta_{a,5-b}$ is a constant antisymmetric matrix. Given $P_a(u)$, the two preceding equations give a homogeneous finite difference equation which can be solved for $Q_{a|j}(u)$, subject to the boundary condition $Q_{a|j} \underset{u\to\infty}{\sim} u^{M_a+\hat{M}_j+1}$ at large imaginary u. This determines $Q_{a|j}$ as an analytic function in the upper-half-plane, with a sequence of short cuts in the lower-half-plane starting at $u = -\frac{i}{2} + [-2g, 2g]$.

To close the equations, one uses eq. (2.31) together with the values of $Q_{a|j}(u)$ at $u \in \frac{i}{2} + [-2g, 2g]$ to evaluate $Q_j(u)$ for $u \in [-2g, 2g]$ along the real axis. On the sheet shown in fig. 2, the function $Q_j(u)$ has an infinite series of short cuts in the lower-half-plane. A crucial requirement is that if one were to go through the first short cut at $[-2g, 2g]$, one would find a function $\tilde{Q}_j(u)$ that is analytic in the lower-half-plane. For the symmetrical operators that we consider in (2.26), we use the gluing conditions in (5.13) of [18] (with $\beta = \gamma = 0$ therein),

$$\tilde{Q}_1(u) = \alpha\, \bar{Q}_3(u) \quad \text{and} \quad \tilde{Q}_2(u) \;= -\alpha^*\, \bar{Q}_4(u) \tag{2.32}$$

where α is a constant (only g-dependent), * is complex conjugation, and the continuation $\tilde{Q}$ is obtained simply by using $\tilde{P}_a$ instead of P_a in (2.31); $\bar{Q}_j(u) \equiv Q_j(u^*)^*$. These can be viewed as relations between analytic functions in the lower-half-plane, which can be analytically from there.

For numerical implementation, following [18] we take (2.32) to the real axis and define the following ratios:[2]

$$\alpha_{13}(u) \equiv \frac{Q_1(u+i0)}{Q_3(u+i0)^*}, \quad \alpha_{31}(u) \equiv \frac{\tilde{Q}_1(u+i0)}{\tilde{Q}_3(u+i0)^*}, \quad \alpha_{24}(u) \equiv -\frac{Q_2(u+i0)^*}{Q_4(u+i0)}, \quad \alpha_{24}(u) \equiv -\frac{\tilde{Q}_2(u+i0)^*}{\tilde{Q}_4(u+i0)}\,. \tag{2.33}$$

These four quantities should be constant (u-independent) and equal to each other. We demand that this holds for a set of N_{cut} sampling points $u_m \in [-2g, 2g]$. These gluing conditions determine the parameters $c_{a,n}$ in (2.27), from which one reads off the scaling dimension from the exponents in (2.24), which are themselves related to the constants $c_{a,0}$.

[2] The identity $\tilde{Q}_j(u - i0) = Q_j(u + i0)$ is helpful to show the equivalence with (2.32), both slightly below $(\alpha_{13}, \alpha_{24})$ and slightly above $(\alpha_{31}, \alpha_{42})$ the real cut.

To solve these conditions we follow the numerical algorithm based on the multivariate Newton's method described in section 6 of [18], as used initially in [34]. This requires to start with a seed of approximate values for the $c_{a,n}$ in eq. (2.27). One then solve the difference equation (2.30)-(2.31) to evaluate the four ratios $\alpha_{jk}(u)$ at a discrete set of m points along the cut. Since all α's should be equal and constant, the variance should vanish:[3]

$$S = \sum_{m=1}^{N_{\text{cut}}} \left|\alpha_{13}(u_m) - \bar{\alpha}\right|^2 + \left|\alpha_{31}(u_m) - \bar{\alpha}\right|^2 + \left|\alpha_{24}(u_m) - \bar{\alpha}\right|^2 + \left|\alpha_{42}(u_m) - \bar{\alpha}\right|^2 \tag{2.34}$$

where $\bar{\alpha}$ is the mean value of the list $\{\alpha_{13}(u_m),\, \alpha_{31}(u_m), \alpha_{24}(u_m),\, \alpha_{42}(u_m)\}$. The multivariate Newton method minimizes S iteratively as

$$\{c_{a,n}\} \longrightarrow \{c_{a,n}\} + \{\delta c_{a,n}\}_{\text{Newton Shift}} \tag{2.35}$$

where the changes in parameters are estimated from the derivatives $\frac{\partial \alpha_{jk}(u_m)}{\partial c_{a,n}}$ (estimated numerically by varying each $c_{a,n}$ by a small amount ϵ), similar to [18]. By iterating the algorithm several times starting from an adequate seed, the parameters $\{c_{a,n}\}$ converge to a value which solves the QSC equations with high accuracy. The algorithm and the parameters involved at each step are summarized in table 1.

We benefit from the fact that the algorithm has been extensively applied already to low-lying operators. Results for the Konishi operator will be described below. Later in [35], the same algorithm was used to produce data for higher spin operators $J = 2, 4, 6$, for a large range of coupling values $g \in [0.1, 8]$. In figure 3 we show data provided by the ancillary of [35]. We have used this data to test our own code.

For our purposes, we extended this database to include higher spin operators $J = 8, 10, \cdots$ in the leading Regge trajectory and the lightest operator of the first sub-leading trajectory. For this, we need to find good seeds to start the numerical algorithm. We use three complementary ways to find them:

- In [48] we can find a database of solutions to the QSC at weak coupling. The solutions are presented as series expansions in g, see for instance (2.36). We use these results as seeds when the coupling is small $g < 0.25$, which is the typical radius of convergence of perturbation theory for many quantities.

- After generating a list of data for small coupling we can extrapolate to generate seeds for $g > 0.25$. After using the numerical algorithm to refine them, we can extrapolate again to larger and larger values of g.

- We can also extrapolate on the spin J and move along a Regge trajectory for a fix value of the coupling. This is possible after producing a database for a few spins, such as the one provided in [35].

[3] It was observed that the α_{13} and α_{31} gluing conditions suffice to determine leading-twist operators [34]. For subleading trajectories, we observe that the four terms in (2.34) are essential to lift unconstrained directions in parameter space and ensure numerical stability.

	Description
P_a **Ansatz**	Start with a guess $\{c_{a,n}\}_{\text{seed}}$ in (2.27) truncated at order $n_{\max} = N_p$.
Glueing conditions	Find the series $Q_{a,j}^{\text{large}} = u^{M_a+\tilde{M}_j+1} \sum_{n=0}^{N_q} \frac{b_{a,j,n}}{u^{2n}}$ by solving (2.30) given $\{c_{a,n}\}$. Iterate (2.24) to find $Q_{a,j}(u_m + \frac{i}{2})$ starting from $Q_{a,j}^{\text{large}}(u_m + \frac{i}{2} + iu_\infty)$. Use (2.31) to find $Q_j(u_m)$, $\tilde{Q}_j(u_m)$ and $\alpha_{ij}(u_m)$ at N_{cut} points on the cut.
Update $\{c_{a,n}\}$	Evaluate the errors $\alpha_{ij}(u_m)$ for parameters that differ by ϵ, and use Newton's method to update $\{c_{a,n}\}$.

Table 1: Summary of steps and parameters in numerical algorithm for QSC. The last step is repeated until coefficients $\{c_{a,n}\}$ are found which minimize the error $\sum_{m=1}^{N_{\text{cut}}} |F(u_m)|^2$ for the chosen parameters N_p, N_q, u_∞ and N_{cut}. We normally choose those such that the dominant error is from N_p.

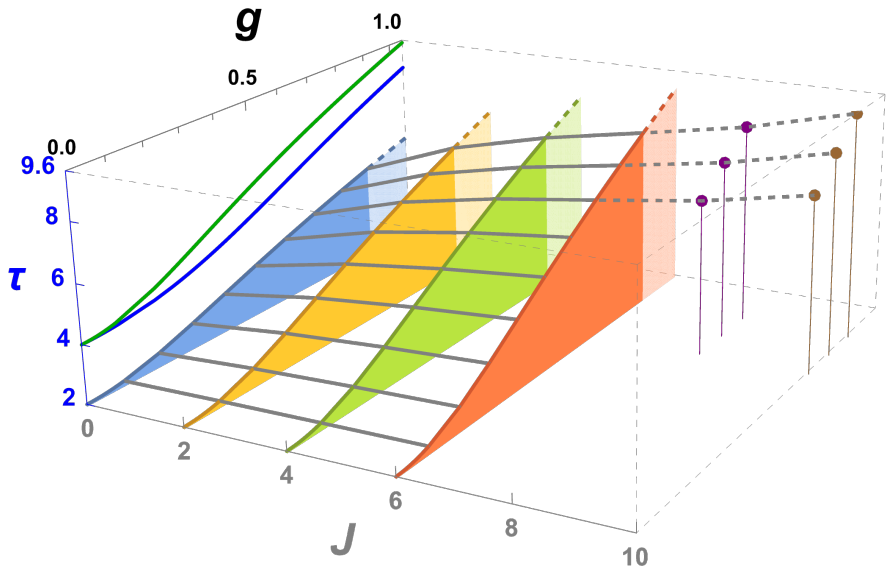

Figure 3: Scaling dimension for operators along the leading Regge trajectory at various values of the coupling, and for the first two subleading spin-0 operators.

The operators on the subleading trajectory have been less studied but we can obtain seeds using the code from [48] which solves the QSC as a weak coupling series. There are two nearly degenerate operators at spin 0 and twist near 4, whose scaling dimensions are respectively:

$$\begin{aligned}\Delta &= 4 + (13 - \sqrt{41})\, g^2 + 2.413866\, g^4 + \mathcal{O}(g^6)\\ \Delta' &= 4 + (13 + \sqrt{41})\, g^2 - 94.41387\, g^4 + \mathcal{O}(g^6).\end{aligned}$$

The seed corresponding to the first operator is recorded in (A.5). We observe using the quantum spectral curve that the spacing between the two operators continues to increase with coupling in the range of interest in this paper, so they do not cross. To confirm that these operators are indeed the ones corresponding to our problem, we constructed their eigenfunction and leading order structure constants as discussed in (A.7):

$$C_{\Delta}^2 = \frac{3}{640}\left(7 + \frac{27}{\sqrt{41}}\right) + O(g^2), \qquad C_{\Delta'}^2 = \frac{3}{640}\left(7 - \frac{27}{\sqrt{41}}\right) + O(g^2)\,. \tag{2.36}$$

We compared this data with the leading-logarithm terms in our four point correlator expanded to three loops using [49] (minus the contribution from twist-two operators):

$$\begin{aligned}C_{\Delta}^2 u^{\frac{\Delta}{2}} + C_{\Delta'}^2 u^{\frac{\Delta'}{2}}\big|_{\text{leading log}} &= \tfrac{2}{15} + \tfrac{7}{15} g^2 \log u + \tfrac{9}{10} g^4 \log^2 u + \tfrac{23}{10} g^6 \log^3 u + O(g^8 \log^4 u),\\ (\mathcal{H} - \text{twist } 2)\big|_{\text{leading log}} &= 0 + \tfrac{-1}{5} g^2 \log u + \tfrac{9}{10} g^4 \log^2 u + \tfrac{23}{10} g^6 \log^3 u + O(g^8 \log^4 u, z, \overline{z}).\end{aligned} \tag{2.37}$$

The first two terms are not expected to match due to double-trace contributions, but the perfect agreement of the $\log^2 u$ and $\log^3 u$ terms nontrivially confirms that we correctly identified the exchanged operator.

At large spin, we use that operators in the leading Regge trajectory have a universal anomalous dimension with logarithmic scaling:

$$\tau(J)_{\text{twist-2},\, J\to\infty} = 2 + 2\Gamma_{\text{cusp}}(g)\, \log\left(J e^{\gamma_E}\right) + 2\Gamma_{\text{virtual}}(g) + O(\log^{\#}(J)/J) \tag{2.38}$$

$$= 2 + 2\Gamma_{\text{cusp}}(g)\, \log\left(\left(J + \tfrac{\tau+3}{2}\right) e^{\gamma_E}\right) + 2\Gamma_{\text{virtual}}(g) + O(\log^{\#}(J)/J^2). \tag{2.39}$$

The cusp anomalous dimension, which also controls the UV divergences of lightlike cusped Wilson loops, and virtual anomalous dimension are computed by the formulas recorded in (A.2)-(A.3). We use the second version of the formula, in which twist is expressed as a function of the conformal Casimir, and which can be solved iteratively for τ. It is more accurate since it automatically removes $1/J$ corrections [50–52]. In addition, we can compute the gap between the leading and first subleading trajectory at large spin by adding excitations over the so-called GKP string, which represents the reference state corresponding to large spin operators:

$$\tau(J)_{\text{twist-4},\, J\to\infty} = 2 + 2\Gamma_{\text{cusp}}(g)\, \log\left(J e^{\gamma_E}\right) + 2\Gamma_{\text{virtual}}(g) + \Delta\tau_{J\to\infty}(g). \tag{2.40}$$

The lightest R-singlet excitations is a pair of zero-momentum scalars, $\Delta\tau_{J\to\infty}(g) = 2E_{\phi}(g)$, whose energy is calculated from eq. (A.4). The raw data we use from integrability are summarized in table 2.

	$g = 0.1$	$g = 0.2$	$g = 0.3$
$\tau(J = 0)$	2.115506378	2.418859881	2.826948662
$\tau(J = 2)$	2.160267638	2.580161632	3.144804548
$\tau(J = 4)$	2.188431616	2.681905193	3.346021685
$\tau(J = 6)$	2.209027779	2.756495396	3.493970284
$\tau(J = 8)$	2.225274740	2.815455912	3.611191520
$\tau(J = 10)$	2.238693733	2.864235300	3.708355788
$\Delta\tau(J = 0)$	1.950671369	1.846969572	1.768329035
Γ_{cusp}	0.03877086865	0.1433749321	0.291663365
$2\Gamma_{\text{virtual}}$	−0.00267496013	−0.03534213604	−0.139719169
$\Delta\tau(J\to\infty)$	1.895980997	1.645777840	1.351463213

Table 2: Spectral data for the leading Regge trajectory and gap to the first subleading trajectory, used for numerical bootstrap. These include the twists obtained from the Quantum Spectrum Curve, as well as large-spin asymptotics from the asymptotic Bethe Ansatz.

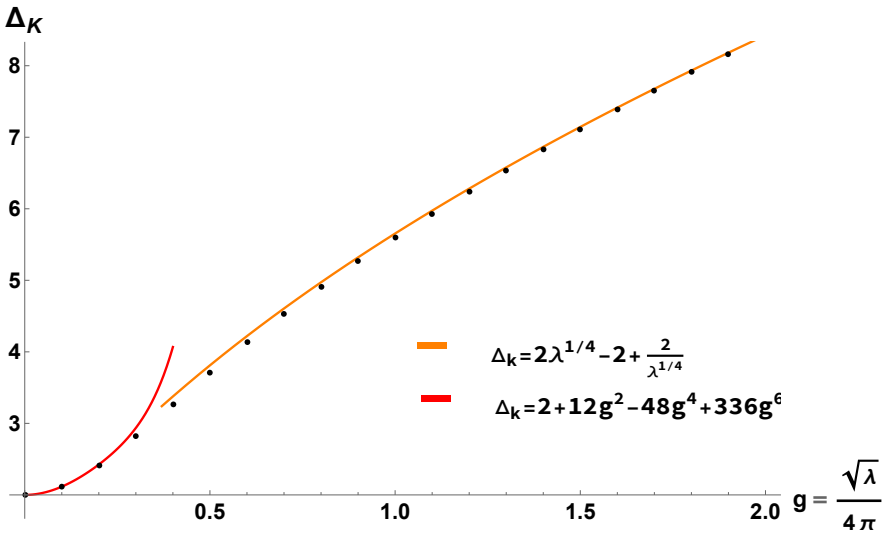

Figure 4: Scaling dimension of the Konishi operator at finite coupling, using data $g \in [0, 2]$ from [35]. This was originally plotted in [15] . We also include comparison with the first 3 terms at weak and strong coupling, which were originally obtained in [32] and [33] respectively.

2.4 Properties of the Konishi operator at weak and strong coupling

The Konishi operator will be particularly important in our study since its scaling dimension effectively defines the 't Hooft coupling, from the point of view of the correlation function we are studying; bounding its OPE coefficient will be our main focus.

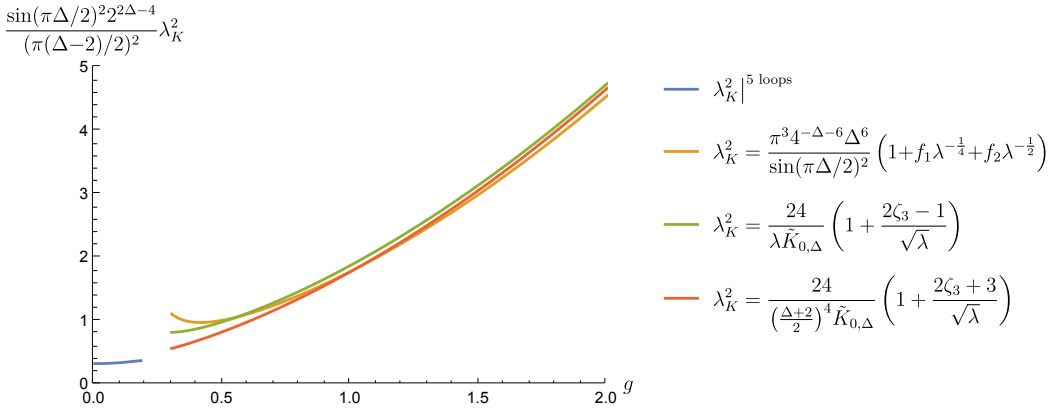

Figure 5: Rescaled OPE coefficient of the Konishi operator to two stress tensor multiplets at weak (2.42) and strong coupling (2.44). We display three forms of the strong coupling formula, which agree at asymptotically large g but become distinct at intermediate g. The rescaling was applied to remove oscillations and the overall exponential trend.

At weak coupling, the scaling dimension of the Konishi operator has been provided to 11 loop orders in [48] (building on much earlier work referenced there). We reproduce here the first 5 orders:

$$\begin{aligned}\Delta_K = 2 &+ 12g^2 - 48g^4 + 336g^6 + g^8(576\zeta_3 - 1440\zeta_5 - 2496)\\ &+ g^{10}\left(6912\zeta_3 - 5184\zeta_3^2 - 8640\zeta_5 + 30240\zeta_7 + 15168\right) + \mathcal{O}(g^{12}).\end{aligned} \tag{2.41}$$

Its OPE coefficient is currently know to 5 loop orders [36]:

$$\begin{aligned}\lambda_K^2 = &\frac{1}{3} - 4g^2 + g^4(56 + 24\zeta_3) + g^6(-768 - 128\zeta_3 - 400\zeta_5)\\ &+ g^8(9952 + 1312\zeta_3 + 288\zeta_3^2 + 3920\zeta_5 + 5880\zeta_7)\\ &+ g^{10}(-117824 - 28992\zeta_3 + 6624\zeta_3^2 - 43008\zeta_5 - 13824\zeta_3\zeta_5 - 59472\zeta_7 - 84672\zeta_9)\\ &+ \mathcal{O}(g^{12}).\end{aligned} \tag{2.42}$$

Recall that we removed an overall factor $\frac{1}{c}$ from our OPE coefficients, see eq. (2.11).

At strong coupling, the scaling dimension is known to 3 loop order ($\lambda^{-5/4}$) from [53],

$$\Delta_K = 2\lambda^{\frac{1}{4}} - 2 + 2\lambda^{-\frac{1}{4}} + \left(\frac{1}{2} - 3\zeta_3\right)\lambda^{-\frac{3}{4}} + \left(\frac{1}{2} + 6\zeta_3 + \frac{15}{2}\zeta_5\right)\lambda^{-\frac{5}{4}} + O(\lambda^{-\frac{7}{4}}), \tag{2.43}$$

while the OPE coefficient is known through its relation to the Virasoro-Shapiro amplitude [9, 10, 37]. Recently, ref. [54] also obtained subleading corrections by adding spectral information

from integrability, together with constraints from localization:

$$\begin{aligned}\lambda_K^2 &= \frac{\pi^3 \Delta_K^6}{4^{\Delta_K+6}\sin\left(\frac{\pi\Delta_K}{2}\right)^2}\left(1+f_1\lambda^{-\frac{1}{4}}+f_2\lambda^{-\frac{1}{2}}+O(\lambda^{-\frac{3}{4}})\right)\\ &= \frac{24}{\lambda \tilde{K}^{N=4}_{0,\Delta_K}}\left(1+\frac{2\zeta_3-1}{\sqrt{\lambda}}+O(\lambda^{-1}\right), \end{aligned} \tag{2.44}$$

where $f_1 = \frac{23}{4}$ and $f_2 = \frac{405}{32}+2\zeta_3$ on the first line.[4] The second line is an equivalent rewriting of the formula using the factor $\tilde{K}^{N=4}$ defined below (C.14), which arises naturally in the derivation of the coefficient. Note that this rewriting neatly removes the $\lambda^{-\frac{1}{4}}$ term. We thus expect the second series to proceed in integer powers of $1/\sqrt{\lambda}$, which would be interesting to verify.

The quantum spectral curve reviewed above enables to compute the scaling dimension Δ_K numerically with arbitrary precision at any g. Figure 4 displays the resulting curve from the original article [34], along with its comparison with weak and strong coupling expansions.

It is amusing to similarly plot the weak and strong coupling predictions for the OPE coefficient, for which exact results are not yet available. Since (2.44) depends strongly on the coupling g, different forms which agree asymptotically become distinct at moderate g, as visible in figure 5. (Without the subleading terms in (2.44), the curves would differ from each other much more strongly.) Below we study the OPE coefficient at $g = 0.3$. It is hard to extract a definite value from the plot, but it seems reasonable to assume that the true value should lie somewhere between a linear extrapolation of the weak coupling curve and the lowest of the strong coupling curve, giving $\lambda_K^2(g=0.3) \in [0.24, 0.33]$ (corresponding to the range $[0.4, 0.55]$ in the rescaled plot).

3 A menu of functionals

All functionals we consider in this work are combinations of the Polyakov-Regge crossing equation $X_{u,v}$ (2.20) and antisubtracted B_v-sum rule (2.21). As detailed in the next section, we will seek linear combinations which are positive on every possible state in the spectrum, and which maximize certain objectives. Since the space of functionals to explore is infinite-dimensional, different truncations can exhibit different numerical properties.

In this section we define some infinite linear combinations of the $X_{u,v}$ and B_v: the Mellin-transformed functionals $\widehat{X}_{\mathrm{s,t}}$ and $\widehat{B}_{\mathrm{t}}$, and special linear combinations $\Phi_{\ell,\ell+2}$ and Ψ_ℓ of B_v which diagonalize its action near twist two. Although these functionals are infinite linear combinations of each other, no finite relations exist, and so we will treat them as independent for numerical purposes.

Generally, a basis of functionals for the numerical bootstrap needs to have the following properties (see for example [39]):

[4] The first arXiv version of [54] reported a different value for f_2. We are grateful to the authors for communicating sharing with us the corrected value.

1. Swappability: Each functional commutes with the infinite sum over the CFT spectrum, ie. each gives a valid sum rule.

2. Asymptotic positivity of finite linear combinations: finite linear combinations must exist which are positive on all but a finite range of (Δ, J).

3. Completeness, as the number of elements tend to infinity.

The first requirement is clearly essential, and is rigorously satisfied by the $X_{u,v}$ and B_v thanks to the Regge boundedness of correlators and the analysis of [39]. We discuss convergence for Mellin-transformed functionals below, as well as the asymptotic positivity of various functionals.

Our strategy to fulfill the third requirement is to present the numerical optimization solver with a varied menu of functionals, and see which ones it prefers.

3.1 Dispersion relations in Mellin space

We now describe the Mellin formulation of the Polyakov-Regge block and collinear functionals corresponding to eq. (2.20) and (2.21) respectively. This formulation is also convenient for numerical evaluation. It was explained in [39] how the position space dispersion relation is equivalent to a straightforward dispersion relation in Mellin space. The Mellin representation for identical-dimension operators takes the form:

$$\mathcal{H}(u,v) = \iint \frac{ds\,dt}{(4\pi i)^2}\, u^{\frac{s}{2}-\Delta_\phi} v^{\frac{t}{2}-\Delta_\phi} \Gamma\big(\Delta_\phi - \tfrac{s}{2}\big)^2 \Gamma\big(\Delta_\phi - \tfrac{t}{2}\big)^2 \Gamma\big(\Delta_\phi - \tfrac{u}{2}\big)^2 M_{s,t}\,. \tag{3.1}$$

Here s, t, u are the Mellin-Mandelstam variables, which are constrained to satisfy $s+t+u = 4\Delta_\phi$, and from here we set $\Delta_\phi \equiv 4$ as the effective external dimension of our reduced correlator. For example, in the $g \to \infty$ limit, the Mellin amplitude goes to

$$M_{s,t}^{\text{strong}} = \frac{1}{(\frac{s}{2}-3)(\frac{t}{2}-3)(\frac{u}{2}-3)}\,. \tag{3.2}$$

The u-channel Regge behavior of $\mathcal{H}$ (see section 2.1) implies that $\lim_{s'\to\infty} M(s',t') \sim s^{J_*-4}$, where $J_* < 2$ and $t' = t+s-s'$ [38]. In particular the reduced correlator satisfies an unsubtracted dispersion relation:

$$M_{s,t} = \oint \frac{ds'}{2\pi i} \frac{M(s',t')}{s-s'} \tag{3.3}$$

where again $t' = t+s-s'$ and the contour encircles all the poles of M except that at $s' = s$. In fact the above only assumes $J_* < 4$. The stronger expectation $J_* < 2$ at finite coupling implies that an "anti-subtracted" dispersion relation also converges, where we put zeros at some subtraction point:

$$M_{s,t} = \oint \frac{ds'}{2\pi i} \frac{(s'-s_0)(t'-s_0)}{(s-s_0)(t-s_0)} \frac{M(s',t')}{s-s'}. \tag{3.4}$$

A natural choice is $\mathrm{s}_0 = 6$, which suppresses the contribution from twist-two operators. These two relations are not independent, and their equality amounts to the sum rule

$$0 = \frac{1}{(\mathrm{s}-\mathrm{s}_0)(\mathrm{t}-\mathrm{s}_0)} \oint \frac{d\mathrm{s}'}{2\pi i} (\mathrm{s}'-\mathrm{t}) M(\mathrm{s}',\mathrm{t}') \tag{3.5}$$

for any s,t. This constraint is essentially independent of s_0.

The poles of the Mellin amplitude, according to the OPE (2.6), occur at descendants of primaries

$$M(\mathrm{s},\mathrm{t}) \sim \frac{\lambda^2_{\Delta,J} \mathcal{Q}^m_{\Delta+4,J}(\mathrm{t})}{\mathrm{s}-(\Delta+4-J+2m)}\,, \tag{3.6}$$

where $\mathcal{Q}$ is a Mack polynomial discussed further in appendix C.2, and $m \geq 0$ is an integer. Assuming the same spectrum in the s- and t- channel, their contribution can be combined in the form

$$M_{\mathrm{s},\mathrm{t}} = M^{\text{strong}}_{\mathrm{s},\mathrm{t}} + \sum_{\Delta,J} \lambda^2_{\Delta,J} \widehat{\mathcal{P}}^{N=4}_{\mathrm{s},\mathrm{t}}[\Delta,J]\,, \tag{3.7}$$

where the Polyakov-Regge block is defined as

$$\widehat{\mathcal{P}}^{N=4}_{\mathrm{s},\mathrm{t}}[\Delta,J] = \sum_{m=0}^{\infty} \mathcal{Q}^m_{\Delta+4,J}(16-\mathrm{s}-\mathrm{t}) \left[\frac{1}{\mathrm{s}-(\tau+2m+4)} + \frac{1}{\mathrm{t}-(\tau+2m+4)}\right]. \tag{3.8}$$

On the other hand, the constraint (3.5) amounts to the sum rule

$$0 = \widehat{B}^{\text{protected}}_{\mathrm{t}} + \sum_{\Delta,J} \lambda^2_{\Delta,J} \widehat{B}_{\mathrm{t}}[\Delta,J] \tag{3.9}$$

where (without loss of generality) we focus on the residue at $\mathrm{s} = \mathrm{s}_0$ and set $\mathrm{s}_0 = 6$:

$$\widehat{B}^{\text{protected}}_{\mathrm{t}} = \frac{2}{(\frac{\mathrm{t}}{2}-3)(\frac{\mathrm{t}}{2}-2)}, \tag{3.10}$$

$$\widehat{B}_{\mathrm{t}}[\Delta,J] = \sum_{m=0}^{\infty} \frac{2(\Delta-J+2m)+2-t}{t-6} \mathcal{Q}^m_{\Delta+4,J}(10-\mathrm{t}). \tag{3.11}$$

The salient property of these sum rules is that they have double-zeros on all double-trace locations $\Delta = 4+2m+J$, originating from the Mack polynomials. They are similar but distinct from those used recently in [54] to constrain stringy corrections to double-trace OPE data: here we concentrate on sum rules which strictly remove all double-traces.

The Polyakov-Regge expansions (2.17) and (3.7) are formally similar, and our nomenclature is not an accident: a result of [39] is that $\widehat{\mathcal{P}}$ is precisely the Mellin transform of $\mathcal{P}$! This is established using the uniqueness properties of Polyakov-Regge block namely, single-valuedness, Regge boundedness, and the pattern of zeroes on Regge trajectories. Similarly,

B_v and $\widehat{B}_{\rm t}$ are related by a Mellin transform. Explicitly,

$$\mathcal{P}^{N=4}_{u,v}[\Delta,J] = \int_{5-i\infty}^{5+i\infty} \frac{ds\,dt}{(4\pi i)^2} u^{\frac{s}{2}-4} v^{\frac{t}{2}-4} \Gamma\left(4-\tfrac{s}{2}\right)^2 \Gamma\left(4-\tfrac{t}{2}\right)^2 \Gamma\left(4-\tfrac{u}{2}\right)^2 \widehat{\mathcal{P}}^{N=4}_{\rm s,t}[\Delta,J], \tag{3.12}$$

$$B_v[\Delta,J] = \frac{1}{2}\int_{5-i\infty}^{5+i\infty} \frac{dt}{4\pi i} v^{\frac{t}{2}-4} \Gamma\left(4-\tfrac{t}{2}\right)^2 \Gamma\left(\tfrac{t}{2}-1\right)^2 \widehat{B}_{\rm t}[\Delta,J]. \tag{3.13}$$

The physical requirements on these contours is that they run to the left of all s and t-channel poles (so $\mathrm{Re(s)}, \mathrm{Re(t)} < \min(8, \Delta - J + 4)$), and to the right of u-channel poles (so $\mathrm{Re(s+t)} > 8$). Since all operators considered in this paper have $\Delta - J \geq 2$, the simple choice $\mathrm{Re(s)} = \mathrm{Re(t)} = 5$ indicated above works uniformly.

The identities (3.12)-(3.13) are highly nontrivial and give us independent methods to compute functionals numerically. In appendix C, we discuss our current best numerical implementations for each. Roughly, position-space methods seem to scale better with increasing spin, while our Mellin-space implementations scale better with increasing precision and are generally faster. The precise numerical agreement between these independent methods is very helpful for debugging.

As simple consistency check, note that $B_v^{\rm protected}$ and $\widehat{B}_{\rm t}^{\rm protected}$ are indeed Mellin-transform of each other:

$$\frac{1}{2}\int \frac{dt}{4\pi i} v^{\frac{t}{2}-4} \Gamma\left(4-\tfrac{t}{2}\right)^2 \Gamma\left(\tfrac{t}{2}-1\right)^2 \frac{2}{(\frac{t}{2}-3)(\frac{t}{2}-2)} = \frac{v^2-1-2v\log v}{v(1-v)^3} = B_v^{\rm protected}\,. \tag{3.14}$$

For future reference, we also define a s↔u crossing functional in Mellin space as

$$\widehat{X}_{\rm s,t} \equiv \widehat{\mathcal{P}}^{N=4}_{\rm s,t} - \widehat{\mathcal{P}}^{N=4}_{16-{\rm s}-{\rm t},{\rm t}}\,, \tag{3.15}$$

which is the Mellin transform of $X_{u,v}$ in (2.20).

3.2 Projection functionals derived from B_v

So far we have two versions of the collinear functional, B_v and $\widehat{B}_{\rm t}$, which diagonalize respectively a position cross-ratio or a Mellin moment. It is natural to try to diagonalize other quantities, for example the action operators of twist close to two and various spins. Since twist-two operators dominate dispersive sum rules at weak coupling, up to $\sim g^4$ contributions from operators of twists $\tau \geq 4$, these functionals effectively solve the 1-loop problem analytically. They could also potentially be useful to suppress large-spin contributions.

Such *projection functionals* can be constructed by integrating $\widehat{B}_{\rm t}$ against a kernel $W[{\rm t}]$:

$$W[\Delta,J] \equiv \int \frac{dt}{4\pi i} W[{\rm t}] \widehat{B}_{\rm t}[\Delta,J]. \tag{3.16}$$

These can be thought of as an infinite sums of collinear functionals finely tuned to possess desirable properties.

We constructed the following projectors, labelled by even spins $\ell \geq 0$, whose details can be found in appendix B. They are characterized by their zeros near twist two:

1. The $\Phi_{\ell,\ell+2}$ functional (B.25) has simple zeros at $\tau = 2$ for $J = \ell$ or $\ell+2$, and double zeros on all other spins:

$$\lim_{\tau\to 2} \Phi_{\ell,\ell+2}[\tau + J, J] = 0 + (\tau - 2)\left(\delta_{\ell,J} - \frac{\Phi^{\infty}_{\ell}}{\Phi^{\infty}_{\ell+2}}\delta_{\ell+2,J}\right) + O((\tau-2)^2)\,. \tag{3.17}$$

2. The Ψ_ℓ functional (B.35) has double-zeros for all spins except $\ell = J$, where it has a nonvanishing intercept and slope:

$$\lim_{\tau\to 2} \Psi_{\ell}[\tau + J, J] = \delta_{\ell,J}\,(1 + (\tau-2)\beta_\ell) + O((\tau-2)^2)\,. \tag{3.18}$$

All these functionals have double-zeros on double traces with $\tau \geq 4$, as required for our applications: they are saturated by single-trace operators at large N_c. The first was inspired by the Φ_ℓ functional used in [39] to prove the existence of operators below the double-twist threshold and fixed spin.

Assuming that the above functionals exist, it is not hard to guess the values of the constants Φ^{∞}_{ℓ} and β_ℓ by expanding the sum rules at weak coupling. The anomalous dimensions for the leading family of long operators have been known for some time (see [55–57] for three-loop results):

$$\Delta(J) - J = 2 + 8g^2 S_1(j+2) + O(g^4), \tag{3.19}$$

$$C(J) \equiv \lambda^2_{\Delta(J),J} = \frac{2\Gamma\left(\frac{\Delta_J+J+4}{2}\right)^2}{\Gamma(\Delta_J + J + 3)}\left(1 - 4g^2 S_2(j+2) + O(g^4)\right)\,, \tag{3.20}$$

where $J \geq 0$ and $S_a(m)$ denote harmonic sums $S_a(m) \equiv \sum_{k=1}^{m} \frac{\text{sign}(a)^k)}{k|a|}$. The stress tensor multiplet is formally the $J = -2$ member of this family, but it is included in the "protected" part[5]. Our focus is on long operators, which have $J \geq 0$. Denoting as $Y^{(i)}$ the coefficient of $(g^2)^i$ in the quantity Y, the data can be expanded as

$$C^{(0)}_J = \frac{2\Gamma(J+3)^2}{\Gamma(2J+5)}, \qquad \gamma^{(1)}_J = 8S_1, \qquad \frac{C^{(1)}_J}{C^{(0)}_J} = \Big[8S_1(j{+}2) - 8S_1(2j{+}4) - 4S_2(j{+}2)\Big]\,. \tag{3.21}$$

Generally, each of the above functionals yields a sum rule on single-trace data of the form

$$0 = W^{\text{protected}} + \sum_{(\Delta,J)\ \text{long}} \lambda^2_{\Delta,J} W[\Delta, J] \tag{3.22}$$

with $W = \Phi_{\ell,\ell+2}$ or Ψ_ℓ. The respective protected parts follow immediately from the protected OPE (3.20)

$$\Phi^{\text{protected}}_{\ell,\ell+2} = 0, \qquad \Psi^{\text{protected}}_{\ell} = -C^{(0)}_{\ell}\,. \tag{3.23}$$

[5] The protected contribution $\widehat{B}^{\text{protected}}_{\text{t}}$ in (3.10) is precisely the analytic continuation of $C^{(0)}_J \widehat{B}_{\text{t}}[J+2, J]$ to $J = -2$.

The salient feature of all sum rules we consider is their double zeros at twists 4,6,.... This means that at one-loop the sum rules are saturated by the twist-two family, which we can evaluate from (3.17) and (3.18):

$$\sum_{(\Delta,J)\ \text{long}} \lambda^2_{\Delta,J}\Phi_{\ell,\ell+2}[\Delta,J] = g^2\left(C^{(0)}_\ell\gamma^{(1)}_\ell - \frac{\Phi^\infty_\ell}{\Phi^\infty_{\ell+2}}C^{(0)}_{\ell+2}\gamma^{(1)}_{\ell+2}\right) + O(g^4), \tag{3.24}$$

$$\sum_{(\Delta,J)\ \text{long}} \lambda^2_{\Delta,J}\Psi_{\ell}[\Delta,J] = C^{(0)}_\ell + g^2\left(C^{(1)}_\ell + \beta_\ell C^{(0)}_\ell\gamma^{(1)}_\ell\right) + O(g^4)\,. \tag{3.25}$$

Thus, consistency of the bootstrap sum rule (3.22) with the known perturbative data requires that $C^{(0)}_\ell\gamma^{(1)}_\ell \propto \Phi^\infty_\ell$ with an ℓ-independent factor, and that $C^{(1)}_\ell/(C^{(0)}_\ell\gamma^{(1)}_\ell) = -\beta_\ell$. This is in precise agreement with the constants Φ^∞_ℓ and β_ℓ that come out of the derivation, recorded in eqs. (B.24) and (B.34). In other words, the Φ and Ψ sum rules analytically bootstrap the one-loop theory.

The fact that the one-loop data is determined by crossing was first noticed from large spin expansions in [52], and later extended to finite spin [58]. This is a quite generic behavior, which generally works up to a finite number of constants. For $\mathcal{N}=4$ sYM the one-loop corrections are fixed up to a single overall factor g^2. The novel feature here is that this is obtained from sum rules with nice sign properties (the Ψ_ℓ are non-negative, see appendix B.5), thereby uplifting the one-loop approximations to nonperturbative inequalities. In general, the action of the projection functionals $\Phi_{\ell,\ell'}[\Delta,J]$ and $\Psi_\ell[\Delta,J]$ on an arbitrary state can be calculated exactly using the formulas for Mack polynomials (C.20).

3.3 Convergence of Mellin functionals

It is interesting to consider the sum rules $\widehat{X}_{\mathrm{s,t}}$ and $\widehat{B}_{\mathrm{t}}$ on their own right, rather than simply Mellin representations of position-space sum rules. A crucial fact that is that they are saturated by single-traces in the planar limit, which makes them sensible for our purposes. This can be seen from the Mack polynomials $\mathcal{Q}_{\Delta+4,J}$, which have double zeros when $\Delta-J=4+2n$ with $n\geq 0$; physically this happens because the Γ-functions in the Mellin representation (3.12), (3.13) already account for double-twist operators. To use Mellin functionals, we need to determine the range of s,t such that the functionals can be swapped with the OPE.

Regge boundedness ensures that the functionals converge at large twist. Swappability with respect to the OPE therefore requires that the sum over spin converges.

Let us first consider the $\widehat{B}_{\mathrm{t}}$ functional. Given eq. (3.10), the protected part of this sum rule, we expect convergence to be bounded by the strip $4<\mathrm{t}<6$. We can verify convergence of the OPE explicitly by taking the large spin and fixed twist limit of the Mack polynomials:

$$\widehat{B}_{\mathrm{t}}[\tau+J,J] \propto \mathcal{Q}^m_{\Delta,J}(6-2m+\mathrm{t}-\tau) \sim J^{-11/2+\mathrm{t}-\tau}(...) + J^{5/2-\mathrm{t}}(...). \tag{3.26}$$

The above suggest that the domain of convergence is saturated by the lowest-twist operator. Since the OPE coefficients scale as $\lambda^2_{\Delta,J}\sim J^{1/2}$, we conclude that swappability is guaranteed

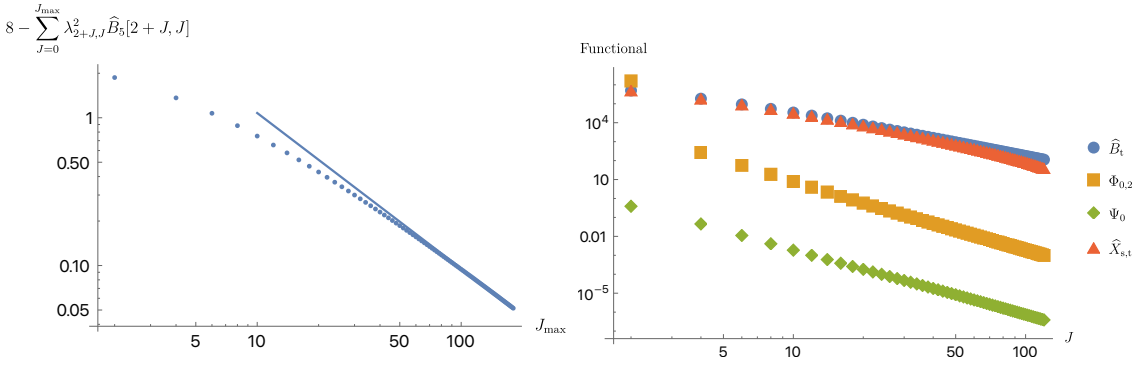

Figure 6: Left: Convergence of the $\widehat{B}_{\rm t}$ sum rule at zero-coupling. We plot the difference between the sum rule and the protected part for $\rm t = 5$ at twist $\tau = 2.001$. The partial sum converges with $J_{\rm max}^{-1.05}$ as shown by the solid blue line in the plot. Right: Convergence at large spin of the Mellin-space functionals for fixed twist $\tau = 2.001$ without the $2\sin^2(\pi\tau/2)$ factor. We normalized the action of all functionals with respect to the collinear $\widehat{B}_{\rm t}$ functional. Furthermore, we evaluated the collinear $\widehat{B}_{\rm t}$ functional at $\rm t = 5$, and the crossing equation sum rule $\widehat{X}_{\rm s,t}$ at $\rm s = t = 5.01$. The collinear functional $\widehat{B}_{\rm t}$ dominates at large spin. The convergence rate α for $J^{-\alpha}$ of the $\widehat{B}_{\rm t}$, $\Phi_{0,2}$, Ψ_0, and $\widehat{X}_{\rm s,t}$ functionals are 2.45, 3.55, 3.54, and 3.97 respectively.

provided that $4 < \rm t < 6$. This is further verified numerically at zero-coupling in the left plot of fig. 6. (A similar conclusion was reached in appendix B of [54].) This exercise further demonstrates that the convergence rate is fixed by the Mack polynomials at large spin, and therefore it is invariant under Regge boundedness (anti)subtractions.

For $\widehat{X}_{\rm s,t}$, the arguments of the Mack polynomials are now dependent on both Mellin-Mandelstam variables s and t. A natural expectation is that convergence is allowed within the triangle-shaped domain $\text{Re}\,\rm s,t,u < 6$, which includes the symmetrical point $\rm s = t = u = \frac{16}{3}$. By evaluating the Mack polynomials in the fixed twist and large spin limit, we find that the forward-channel, the $(\rm s \leftrightarrow u)$ crossed-channel, and the $(\rm t \leftrightarrow u)$ crossed-channel blocks scale as follows:

$$\widehat{P}_{\rm s,t}[\tau+J,J] \propto \mathcal{Q}^m_{\Delta,J}(-2m+\rm s+t-\tau) \sim J^{-23/2+s+t-\tau}(\ldots) + J^{17/2-s-t}(\ldots), \quad (3.27a)$$

$$\widehat{P}_{16-\rm s-t,t}[\tau+J,J] \propto \mathcal{Q}^m_{\Delta,J}(16-2m-\rm s-\tau) \sim J^{9/2-s-\tau}(\ldots) + J^{-15/2+s}(\ldots). \quad (3.27b)$$

$$\widehat{P}_{\rm s,16-s-t}[\tau+J,J] \propto \mathcal{Q}^m_{\Delta,J}(16-2m-\rm t-\tau) \sim J^{9/2-t-\tau}(\ldots) + J^{-15/2+t}(\ldots). \quad (3.27c)$$

After accounting for the OPE coefficient and setting $\tau = 2$, we conclude that the domain of convergence perfectly matches the triangle-shaped strip with $\text{Re}\,\rm s,t,u < 6$!

While we are unable to obtain an analytic expression for the asymptotics of the projected functionals, their growth is expected to be bounded by the collinear $\widehat{B}_{\rm t}$ functional given the

Functional	Range	Protected part	Equation(s)
$X_{u,v}$	(u,v) Euclidean	0	(2.20), (C.27)
B_v	$v>0$ real	$\frac{v^2-1-2v\log v}{v(1-v)^3}$	(2.21), (C.18)
$\widehat{B}_{\mathrm{t}}$	$4<\mathrm{Re(t)}<6$	$\frac{2}{(\frac{\mathrm{t}}{2}-3)(\frac{\mathrm{t}}{2}-2)}$	(3.11), (C.17)
$\widehat{X}_{\mathrm{s,t}}$	$\mathrm{Re(s,t,16-s-t)}<6$	0	(3.15), (C.25)
$\Phi_{\ell,\ell+2}$	$\ell\geq 0$ even integer	0	(3.17), (B.37)
Ψ_ℓ	$\ell\geq 0$ even integer	$-\frac{2\Gamma(\ell+3)^2}{\Gamma(2\ell+5)}$	(3.18), (B.42)

Table 3: Complete list of sum rules we used to bootstrap single-trace operators, including their allowed parameter ranges and protected contribution. The Mellin functionals $\widehat{B}_{\mathrm{t}}$ and $\widehat{X}_{\mathrm{s,t}}$ allow complex parameters. We include links to defining equations and to efficient evaluation formulas.

nature of the projection operation. This is confirmed numerically as shown in the right plot of fig. 6.

3.4 List of functionals we used

To summarize this section, we list the complete set of functionals we use to bootstrap single-trace OPE coefficients. In particular, we use both position- and Mellin-space sum rules.

Although these functionals encode the same information in their respective spaces, the labelling of these functionals (cross-ratios (u,v) in position-space versus Mellin-Mandelstam (s,t) in Mellin-space) highlight how this encoding can lead to distinct functionals; generally, we put hats on Mellin functionals.

In each case, we produce a list of functionals by sampling a range of values. When testing functionals on perturbative data, we observe that numerical convergence is best achieved near the crossing-symmetric points, which are: $z=\bar{z}=-1$ for the position-space crossing functionals $X_{u,v}$, $\mathrm{s}=\mathrm{t}=\mathrm{u}=16/3$ for the Mellin-space Polyakov-Regge blocks $\widehat{X}_{\mathrm{s,t}}$, or $v=1$ and $\mathrm{t}=5$ for the Mellin-space collinear functionals B_v and $\widehat{B}_{\mathrm{t}}$ respectively. In principle we could consider derivatives around these points, but for our numerical implementation we find it easier to sample a random selection of points to high numerical accuracy. The list of sum rules with appropriate ranges is recorded in table 3.

4 Numerical bootstrap

In this section we describe numerical bounds on OPE coefficients obtained using the functionals discussed in the preceding sections, given information about the single-trace spectrum. We focus on the coefficient of the lightest unprotected scalar, the Konishi operator, at weak and strong(ish) values of the coupling: $g=0.1$ and $g=0.3$.

4.1 Generalities

The main concept is similar to OPE bounds in the numerical conformal bootstrap: we look for combinations of functionals that have a definite sign on all allowed states. The main difference is our choice of basis of functionals. Traditionally, the numerical bootstrap exploits functionals that are derivatives of a crossing equation around the crossing-symmetric point; as reviewed in introduction, these must be projected out to obtained N_c-independent bounds in the planar limit. Rather, we rely on the menu of dispersive functionals in table 3. Since we do not a priori know which one are most effective, we use a sample of all of them. Since the different functionals behave differently in various limits (small twist, large twist, or large spin), this strategy is intended to help the linear optimization problem and minimize computational resources.

Explicitly, let us label as W_k any of the functional shown in table 3 for some particular choice of its parameter. Note that even when functionals allow continuous labels (like (u, v) or (s, t)), we only consider discrete choices that lie in the allowed ranges. By swappability, each functional W_k leads to a valid sum rule:

$$0 = W_k^{\text{protected}} + \sum_{(\Delta,J)\ \text{long}} \lambda^2_{\Delta,J} W_k[\Delta, J], \tag{4.1}$$

and we can take finite linear combinations to get

$$0 = \sum_k \alpha_k \left(W_k^{\text{protected}} + \sum_{(\Delta,J)\ \text{long}} \lambda^2_{\Delta,J} W_k[\Delta, J] \right). \tag{4.2}$$

We then separate the protected part and the target OPE coefficient we want to bound, λ^2_K, and impose that all other terms are positive. Namely, we look for linear combinations α_k such that

$$\sum_k \alpha_k W_k[\Delta', J'] \geq 0 \qquad \forall \quad (\Delta', J') \text{ in single-trace spectrum}, \tag{4.3}$$

any of which proves an inequality

$$-\lambda^2_K \left(\sum_k \alpha_k W_k[\Delta_K, 0] \right) \geq \sum_k \alpha_k W_k^{\text{protected}}. \tag{4.4}$$

The prime in (Δ', J') indicates that the Konishi operator is omitted.

The optimal bound (for a particular finite list of functionals $\{W_k\}$) is thus found by solving a standard linear optimization problem on the decision variables α_k, where one maximizes the right-hand-side subject to the inequalities (4.3) and a suitable normalization condition:

$$\begin{aligned} &\text{maximize} && \sum_k \alpha_k W_k^{\text{protected}} \\ &\text{such that} && \sum_k \alpha_k W_k[\Delta_K, 0] = \pm 1 \text{ and (4.3) holds.} \end{aligned} \tag{4.5}$$

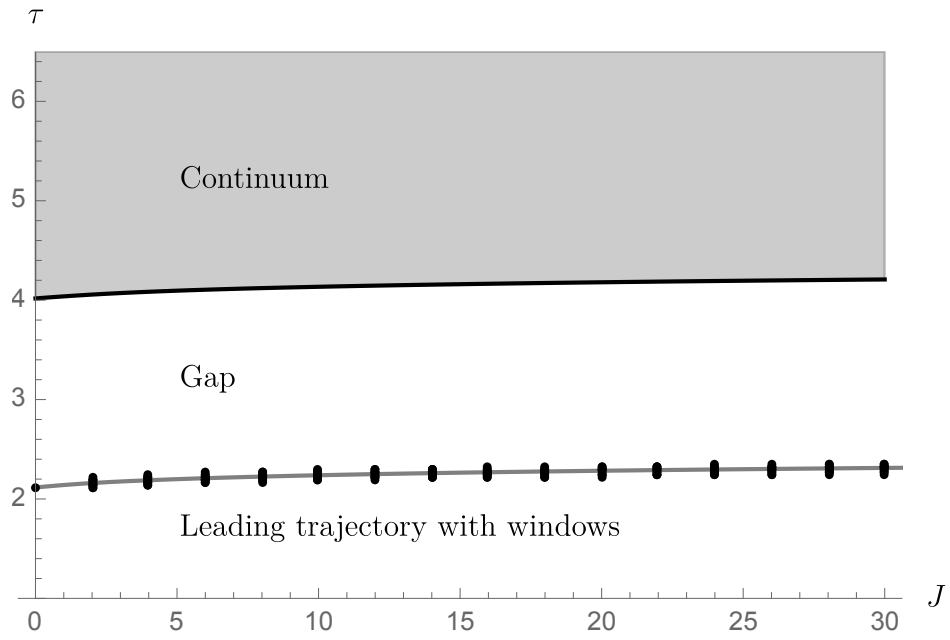

Figure 7: Spectral assumptions for $g = 0.1$. For the leading trajectory, we interpolate between results from integrability at low spins and large spin asymptotics, placing a conservative window around each operator. For subleading trajectories, we demand that the optimized functional be non-negative in a continuum above a twist gap. In this instance, we put exaggerated windows to see if the bootstrap discovers the spectrum.

The plus (minus) sign yields a upper (lower) bound, respectively. We use the SDPB solver to efficiently solve this type of problem [59].

In principle, the inequality (4.3) needs to be imposed on the infinite list of all single-trace operators of the theory. In practice, we can only solve the quantum spectral curve for a finite set, and in any case, we can only solve finite systems of inequalities. Truncation is necessary. Our solution is to identify *ranges* of Δ where operators can be present for each spin, and to impose positivity on a dense sample of discrete values of Δ in that range. Discretization errors can be controlled by plotting the obtained functionals and ensuring that it does not become negative between the sampled points.[6]

Typically, for each spin, we can make good estimates about the leading operator $\Delta_{\text{min}}(J)$ and the gap to the next operator, which we call $\Delta_{\text{thresh}}(J)$. Thus, for each spin, we allow to operators in (4.3) to lie in a small window around $\Delta_{\text{min}}(J)$ (with width determined by our error estimates), or in a continuum at $\Delta > \Delta_{\text{thresh}}(J)$. Our spectral assumptions are further discussed below at weak and strong(ish) coupling.

[6] As is well known and exemplified in the next subsection, optimal functionals typically develop double zeros, whose positions often coincide with those of actual operators. We accept functionals that dip slightly below the real axis between discretization points, as long as their values are small.

Having only an incomplete spectrum implies that the inequalities we find, although conservatively valid, may not be optimal. This discrepancy cannot be removed unless we know the exact spectrum of the theory. Indeed it was observed in the study of 1d defects in $\mathcal{N}=4$ that including more operators improves the numerics significantly [31].

4.2 Bounds at weak coupling: toy problem with 2 functionals

We start our analysis by looking at a toy example with only two functionals, namely Ψ_0 and $\Phi_{0,2}$. Indeed, in the one-loop approximation, these functionals respectively compute the Konishi OPE coefficient (2.42) and the spin-2 anomalous dimension given the Konishi anomalous dimension defined by eq. (2.41). It is thus interesting to ask what they prove at finite but small coupling, ie. $g=0.1$.

Our spectral assumptions are shown in fig. 7. For the leading twist we impose positivity in a large window close to twist 2 without using any perturbative data. We also add a conservative gap of $\Delta\tau=1.9$ between the leading twist and a continuum; this is equal to the asymptotic gap at large spin (see (2.40)), while the gap appears to decrease monotonically with spin.

We find that the optimal combination of these two functionals produces an upper bound that is indeed quite close to the weak coupling OPE coefficient of eq. (2.42), and is almost saturated already by Ψ_0:

$$\begin{aligned} \lambda_K^2(g{=}0.1) &\leq 0.30338 \qquad \text{from } \Psi_0 \text{ alone}, \\ \lambda_K^2(g{=}0.1) &\leq 0.30255 \qquad \text{from } \Psi_0 \text{ and } \Phi_{0,2}. \end{aligned} \tag{4.6}$$

These can be contrasted with the free theory result $\lambda_K^2(g{=}0)=\frac{1}{3}$ and the five-loop prediction $\lambda_K^2(g{=}0.1)^{5-\text{loop}}=0.30067(1)$. We recall that our OPE coefficients have $\frac{1}{c}\approx\frac{4}{N_c^2}$ factored out as shown by eq. (2.11). Bounds with more functionals are discussed in the next subsection.

The optimal two-functional combination is

$$W^{g=0.1}_{\Psi_0+\Phi_{0,2}}=0.90764\Psi_0+0.025498\Phi_{0,2}, \tag{4.7}$$

whose action on the leading trajectory states is displayed in fig. 8. We explicitly see that Ψ_0 nearly saturates the action of this functional.

These bounds, which use functionals optimized for the one-loop problem, improve one-loop perturbation theory in two respects. First, they are numerically closer to the correct answer (in contrast with $\lambda_K^2(g{=}0.1)^{1-\text{loop}}=0.29333$). Second, and perhaps most importantly, they are rigorously valid at finite g.

4.3 Bounds at weak coupling: adding more functionals

It is now interesting to add functionals from table 3 to see if the improved bounds capture higher-loop effects. We consider two options: with 20 functionals and with 40 functionals. Our 20 functionals consist of four Φ_{ℓ_1,ℓ_2}, Ψ_0, as well as five $\widehat{B}_{\text{t}}$ for t evenly spread in the $(4,6)$

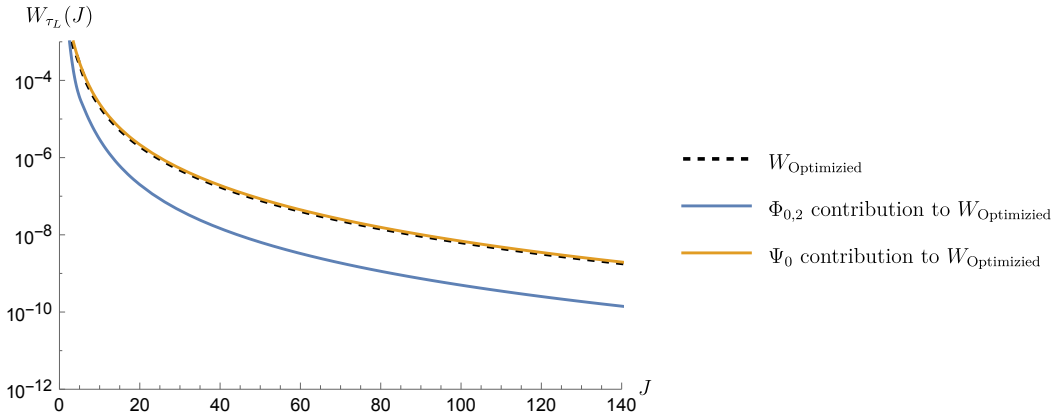

Figure 8: Action of the two-term optimized functional $W^{g=0.1}_{\Psi_0+\Phi_{0,2}}$ on leading trajectory states, showing the relative contributions of Ψ_0 and $\Phi_{0,2}$ (in absolute value). Note the logarithmic scale.

interval. Moreover, we use ten $X_{u,v}$ for a set of u, v satisfying chosen randomly with a flat measure above the $s\leftrightarrow u$ symmetric curve to avoid redundancy.

The largest set of functionals we were able to use consists of 40 functionals including all types from in table 3, except for $\widehat{X}_{s,t}$, which we found challenging to stabilize. In addition to those in the preceding paragraph, we used the Ψ_2, Ψ_4 functionals, nine more $X_{u,v}$, four B_v with v with 0.95, 1.01, 10 and 50, and finally, five more $\widehat{B}_{\text{t}}$. We find that our bounds are stable with respect to adding more $X_{u,v}$'s, however adding more $\widehat{B}_{\text{t}}$ or B_v's could spoil the convergence with twist and spin (and would lead to bounds which rules out the theory). Since $X_{u,v}$ are subdominant at large twist and B's dominates in that region, we suspect that this limitation would be removed if we impose a tighter grid in that region or alternatively use an asymptotic formula.

To obtain robust bounds, we impose positivity up to a large $J_{\text{cutoff}} \sim 6000$ for the leading trajectory and near the gap in the continuum.[7] However, starting $\tau = 20$ we use a smaller cutoff ($J^{\tau>20}_{\text{cutoff}} \sim 250$). We sample twists up to a cutoff $\tau_{\text{cutoff}} \sim 250$. We numerically check that this twist is large enough to ensure positivity on the asymptotic spectrum for the set of functionals considered.

We find that with this increased number of functionals, the upper bound at $g = 0.1$ gets reduced to:

$$\lambda^2_K(g{=}0.1) \leq 0.3018 \qquad \text{from 20 functionals,} \tag{4.8}$$

$$\lambda^2_K(g{=}0.1) \leq 0.3015 \qquad \text{from 40 functionals,} \tag{4.9}$$

again to be compared with the five-loop estimate 0.30067(1). The bound seems stable against increasing the number of $X_{u,v}$ functionals, however it is not clear whether it has converged

[7] To approach J_{cutoff} we extrapolate the functionals after they reach their asymptotic behaviour. For $g = 0.1$ we exactly calculate up to $J \sim 150$ and then extrapolate.

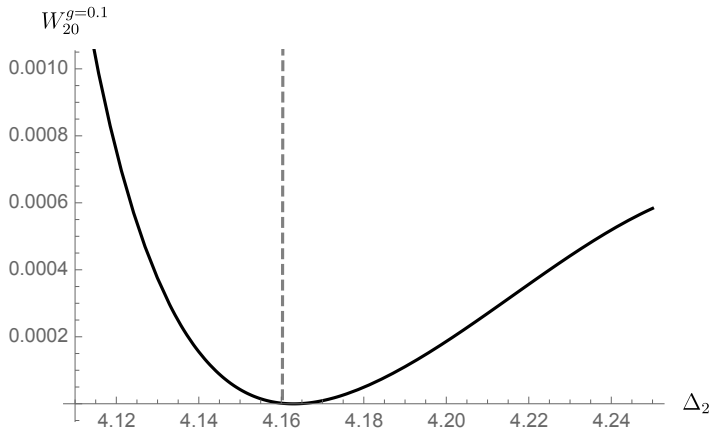

Figure 9: The action of the 20-parameter optimized functional inside the window around the leading-twist spin-2 operator for $g = 0.1$. It displays a double zero at $\Delta \approx 4.164$, where the functional has size $W_{20}^{g=0.1} \sim 10^{-13}$; the vertical dashed line shows the position of the actual operator at $\Delta_2 \approx 4.1603$, where $W_{20}^{g=0.1} \sim 10^{-6}$.

yet with respect to B_v and $\widehat{B}_{\rm t}$ functionals, as mentioned above.

However, as we add more functionals, we gain a higher resolution of the leading-twist spectrum. This means that despite the small change to the upper bound, the optimized functional is in fact manifestly different than the toy model optimized functional.

To investigate our functionals' ability to resolve the spectrum, we put slightly exaggerated windows around the expected position of single-trace operators (from perturbation theory), requiring positivity within these windows. We then observe that the optimal functional develops double zeros at these positions. In fig. 9, we show the optimized functional near $(J, \tau) = (2, 2)$; the double-zero of the optimized functional probes the leading spin-2 single-trace operator in the spectrum. With 20 functionals, we are able to discover the first 6 operators in the leading family. With more functionals one expects of course to discover more states, but we did not try exaggerated windows with 40 functionals, since our main goal was to bound λ_K^2. We have not observed stable double-zeros on the subleading families.

An alternative way to resolve the spectrum is to adjust the size of the positivity window imposed around a given operator; as long as the physical operator lies inside the window, the upper bound on λ_K^2 should not vary. Therefore, by adjusting the upper and lower edges of the positivity window, a kink should form exactly where the operator exits the window. We observe precisely such kinks as shown in fig. 10 for the leading spin-2 operator. Finally, it is worth mentioning that if the window includes the physical operator in the leading family operators, its size does not affect our upper bound at all. Furthermore, omitting windows around operators that are discovered did not change our upper bounds on couplings.

In fig. 11, we illustrate the action of the individual functionals and the optimized one on the leading-twist states. This is qualitatively different from the toy model example considered previously, and the optimized functional is distinct from all individual functionals used in the

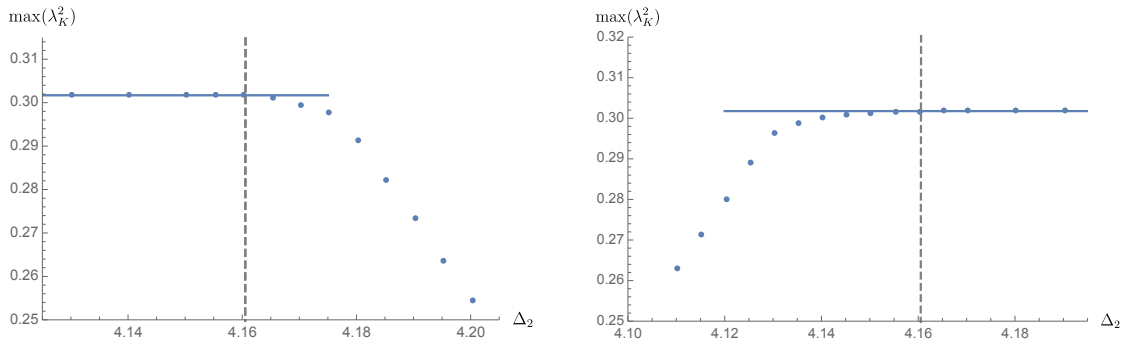

Figure 10: Upper bound on the OPE coefficient of the Konishi operator as a function of the lower edge (left plot) and upper edge (right plot) of the window, using 20 functionals. The other edge was fixed to 4.56 and 3.76 respectively. The horizontal line shows the bound when the window contains the physical spin 2 operator, which is exactly Δ_2-independent. As anticipated from figure 9, the bounds display kinks (non-analyticity) near the physical value of Δ_2, shown as a dashed line.

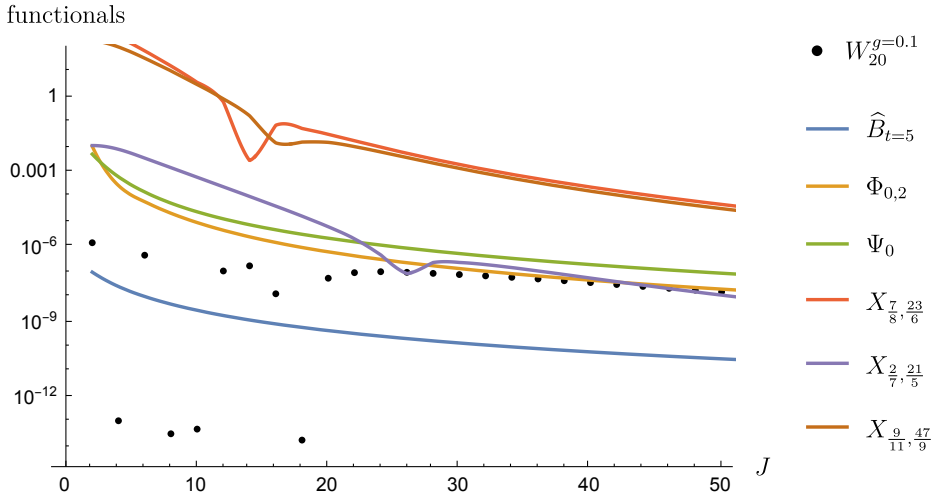

Figure 11: The action of the 20-parameter optimized functional on the states belonging to the leading Regge trajectory for $g = 0.1$, as well as the absolute value of 6 (arbitrarily chosen) individual contributions to it. In contrast to fig. 8, the optimized functional is qualitatively different from any of its individual constituents.

optimization problem.

We repeat our procedure for other weak coupling values such as $g = 0.2$, using the spectral data summarized in table 2. For this coupling, we again find a stable upper bound, essentially independent on the number of functionals:

$$\lambda_K^2(g{=}0.2) \leq 0.26, \tag{4.10}$$

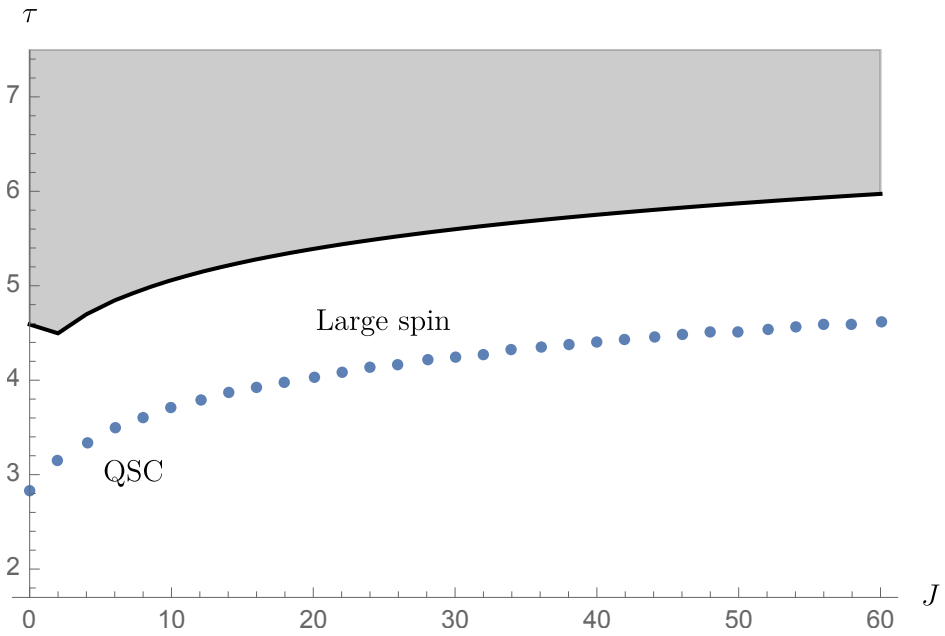

Figure 12: Spectral assumption for $g = 0.3$. We use the QSC results up to spin 10, and for higher spins we use the large-spin asymptotics. Our estimated error is less than 0.0005 for each leading twist operator and is not visible on the plot. For the subleading trajectory, we conservatively use the large-spin gap for $J \geq 2$.

which may be compared with the 5-loop estimate 0.25(2).

Lastly, let's briefly discuss lower bounds on the Konishi operator OPE. Proceeding similarly to the above, we were unable to obtain a non-trivial (nonnegative) lower bound with the set of functionals at hands. We have experimented with including different sets of functionals, as well as with different spectral assumptions and even tried unphysically large twist gaps. We observe that lower bounds converge towards the perturbative value only when we impose an infinite gap for spin 2 and spin 0 operators. What improvements are necessary to obtain a lower bound with realistic spectral assumptions is still an open question.

4.4 Stronger coupling: $g = 0.3$

Having analyzed the weak coupling regime extensively, we are now ready to take the next step and move to values for which perturbation theory is not expected to converge, namely $g > \frac{1}{4}$. As we will see, accurate spectral information becomes increasingly essential.

Our spectral assumptions are shown in fig. 12. For the leading trajectory, we used precise results from the QSC up to spin $J = 10$, followed by the improved large-spin asymptotics (2.39). The latter has an estimated error smaller than 0.0005 for the twist of higher spin states, and even gives per-mil accuracy for $J = 0$! To ensure that our bounds are rigorously valid, we include a window of size ± 0.0005 around each operator up to spin 146.

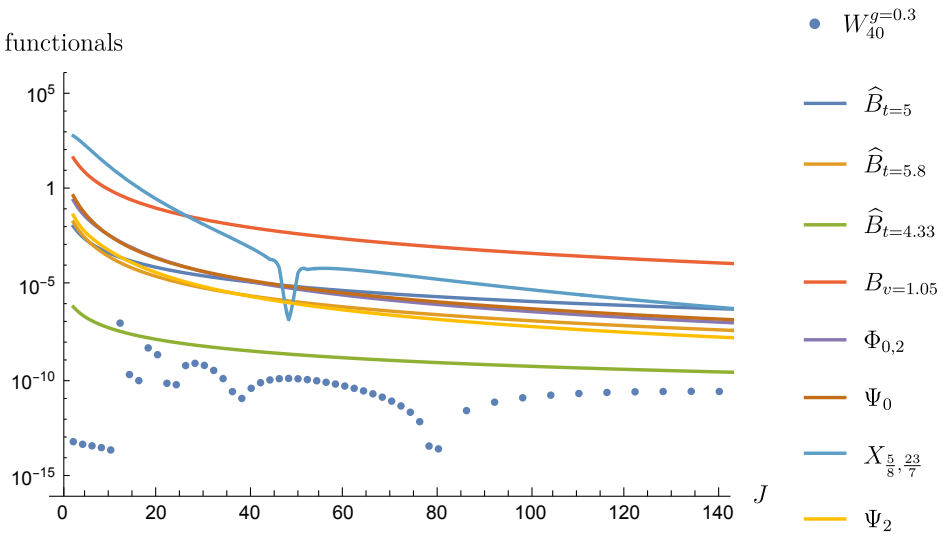

Figure 13: The action of the 40-parameter optimized functional on the states belonging to the leading Regge trajectory for $g = 0.3$, as well as the absolute value of some individual contributions to it.

For the subleading trajectory we use the spin 0 gap derived in table 2, and we use the conservative large spin gap for $J \geq 2$. We use the same J_{cutoff} and τ_{cutoff} as in the preceding subsection. The only difference is that in order to obtain the asymptotic large spin behavior, we need to go higher in spin (as can be seen from comparing fig. 12 and fig. 7). We conservatively choose to calculate up to spin 250 and then extrapolate. We emphasize that we do not have complete control over the large twist, large spin region; for instance, for $20 \leq \tau \leq \tau_{\text{cutoff}}$ we are unable to reach the large-spin asymptotic region and extrapolate. This could potentially affect the rigour of our bound. Further analysis is needed to completely tame this region.

Accurate spectral information seems important. In our earliest attempts, we did not use the improved form of large-spin asymptotics (2.39) which led to much larger error estimates (and larger window sizes $\sim$0.02 near $J = 10$). Using the more accurate spectrum immediately impacted the bounds.

We use the same set of 40 functionals as described at the top of section 4.3. As in the $g = 0.1$ case, the optimal functional does not exhibit zeros near the subleading trajectory, but it exhibits zeros on several operators on the leading trajectory.[8] This is plotted in fig. 13, along with the contributions from some individual functionals.

[8] We did observe nontrivial dependence on the twist gap when using more B functionals, but we could not adequately control the large-spin large-twist region with these functionals.

We quote the result we get with this data to be:

$$\lambda_K^2(g{=}0.3) \leq 0.300 \qquad \text{from 20 functionals,} \tag{4.11}$$

$$\lambda_K^2(g{=}0.3) \leq 0.299 \qquad \text{from 40 functionals.} \tag{4.12}$$

As described at the end of section 2.4, our current best estimates from other methods is $\lambda_K^2(g = 0.3) \in [0.24, 0.33]$. The bound (4.12) exclude the upper part of that range.

5 Discussion

In this paper, we initiated a numerical study of nonperturbative constraints on correlators of four stress tensor multiplets in planar four-dimensional $\mathcal{N} = 4$ sYM. Our methodology consists of three main steps. First, we compute the scaling dimension of low-twist operators using integrability as described in section 2.3; the resulting data that we used is summarized in table 2. Second, we construct dispersive CFT functionals with distinct characteristics as summarized in table 3; each provides a nonperturbative sum rule on planar OPE coefficients. Finally, we implement a numerical bootstrap algorithm to find linear combinations of these sum rules that prove optimal bounds on the desired OPE coefficient, as detailed in section 4.

Our main result is that at small but finite coupling, the OPE coefficient of the Konishi operator satisfies a rigorous upper bound that is nearly saturated by the perturbative series. As a function of other scaling dimensions, the bound displays kinks (see figure 10) which suggest that with more functionals, the optimal bound will be saturated by the theory. At stronger coupling $g = 0.3$, outside the typical domain of convergence of the perturbative expansion, we obtain bounds with conservative spectral assumptions.

We focus on the 't Hooft planar limit since exact spectra from integrability are only available in this limit. On the other hand, this limit is challenging for traditional numerical bootstrap techniques, due to sign-indefinite double-trace contributions. The dispersive functionals described in section 3 avoid this problem by formulating crossing directly at the level of single-trace data, by virtue of having double-zeros that suppress all double-trace operators. We developed new technology to apply dispersive functionals in a numerical bootstrap context, summarized in appendix C, which could be useful for applications to other (non-supersymmetric) conformal field theories.

There is a lot of flexibility in the space of dispersive functionals. We constructed special combinations, the projected functionals $\Phi_{\ell,\ell+2}$ and Ψ_ℓ (see eqs. (3.17)-(3.18)), which isolate specific twist-two anomalous dimensions and OPE coefficients in the weak coupling limit and determine them at one-loop. Significantly, the Ψ_ℓ are nonnegative, which ensure that they prove rigorous bounds at finite coupling. By studying numerically combinations of more functionals, we find extremal combinations that develop double zeros at the location of various operators (see section 4.3), demonstrating that the functionals nonperturbatively constrain the spectrum.

As we increase the coupling and move beyond the convergence radius of perturbation theory, we observe that the optimal functionals become qualitatively different from Φ and

Ψ. A main outstanding challenge to reach larger values of coupling is to gain more analytic control over positivity of the optimal functional in asymptotic regions of large spin and large twist. This will be needed to make completely rigorous the bounds presented in this paper. Furthermore, we expect that this will enable the stable inclusion of more B-type functionals. As discussed in subsection 4.4, this could enable the functionals to probe subleading Regge trajectories, whose scaling dimensions can be provided by the QSC.

We only obtain nontrivial upper bounds on OPE coefficients. This is to be contrasted with the 1D Wilson line defects considered in [30, 31], where tight lower bounds are also obtained. It is possible that with more spectral information or more functionals this situation will improve. An alternative scenario is that, like in the 3D Ising model, bootstrapping the theory down to an isolated island will require to study more correlation functions [60].

Our analysis was performed in the strict planar limit: all the sum rules we used are homogenous in N_c. It could be interesting to compare results with the conventional numerical bootstrap at some large but finite N_c.

We anticipate many possible extensions of our analysis. First, with some optimization it should be possible to find from the QSC the scaling dimension of many more operators, with higher spin and/or higher twist. Second, it might be possible to derive polynomial approximations for the Δ-dependence of dispersive functionals, which would make it possible to include a vastly larger number of functionals. Such approximations were a crucial step in the development of the modern numerical bootstrap [61], and this technology would also be a key step toward applying dispersive functionals to other models. Third, it may be possible to incorporate sum rules beyond those we considered, for example the integrated constraints from localization [7, 62], or constraints from mixed correlators involving other half-BPS operators. It remains to be determined if the method can yield tight two-sided bounds on OPE coefficients.

Acknowledgments

We thank Fernando Alday, Shai Chester, Miguel Paulos, João Silva and David Simmons-Duffin for insightful comments. All authors are supported by the Simons Foundation through the Simons Collaboration on the Nonperturbative Bootstrap. Work of SCH is additionally supported by the Canada Research Chair program and the Sloan Foundation, while AT is further supported by the Natural Sciences and Engineering Research Council of Canada. ZZ is also supported by the Fonds de Recherche du Québec–Nature et Technologies. This research was enabled in part by support provided by Calcul Québec and Compute Canada (Narval and Graham clusters).

A Additional formulas from integrability

To obtained the large-spin asymptotics quoted in table 2, we used the following formulas from the asymptotic Bethe Ansatz, from [63, 64]. The essential step is to build the (infinite)

matrix, which effectively inverts the Beisert-Eden-Staudacher (BES) kernel [65]:

$$\mathcal{K}_{ij} \;=\; (-1)^{(i+1)j} 2j \int_0^\infty dt \frac{J_i(2gt)J_i(2gt)}{t\,(e^t-1)} \tag{A.1}$$

By inverting the matrix $(1+\mathcal{K})$ and dotting into suitable vectors, one finds the cusp and virtual anomalous dimensions

$$\Gamma_{\text{cusp}} = 4g^2 [\, Q \cdot (1+\mathcal{K})^{-1}\,]_{11} \tag{A.2}$$

$$\Gamma_{\text{virtual}} \;=\; 4g\,[\, Q \cdot (1+\mathcal{K})^{-1} \cdot \mathcal{V}]_1\,, \qquad \mathcal{V}_i \;\equiv\; \int_0^\infty dt \frac{J_i(2gt)J_0(2gt) - g\,t\,\delta_{i1}}{t\,(e^t-1)}\,. \tag{A.3}$$

with $Q_{ij} = j(-1)^{j+1}\delta_{i,j}$. Similarly, the ground state energy of a scalar excitation is

$$E_\phi = 1 + 4g\,[\, Q \cdot (1+\mathcal{K})^{-1} \cdot \mathcal{V}^\phi\,]_1, \qquad \mathcal{V}^\phi_i \equiv \int_0^\infty dt \frac{J_i(2gt)(J_0(2gt) - e^{\frac{t}{2}})}{t(e^t-1)}. \tag{A.4}$$

In practice, these are calculated by truncating the matrix $\mathcal{K}$ to a finite size and extrapolating the results to infinite size. For the relatively small values of the coupling that we consider, convergence is fast.

Since the leading twist-4 operator has not been discussed earlier, we also record weak coupling QSC data corresponding to it, extracted from the code of [48] solved with quantum numbers $\{\{0,0\},\{2,2,2,2\},\{0,0\}\}$ (after rescaling and shifting P_3^{there} by a multiple of P_1^{there} to make explicit the left-right symmetry of the QSC)

$$\begin{aligned}
\Delta \;&=\; 4 + 6.60g^2 + 2.41g^4 + \mathcal{O}(g^6) \\
(gx)^2 P_1 \;&=\; (-6.7 - 43g^2 - 100g^4) + \frac{-18g^2 - 98g^4}{x^2} + \frac{0}{x^4} + \frac{0}{x^6} \\
gx P_2 \;&=\; (-36 - 170g^2 - 350g^4) + \frac{-42 - 260g^2 - 960g^4}{x^2} + \frac{-32g^2 - 430g^4}{x^4} + \frac{0}{x^6} \\
P_3 \;&=\; 1 + \frac{\frac{0.34}{g^2} + 3.3 + 4.6g^2 + 9.5g^4}{x^2} + \frac{1.4 + 6g^2 + 3.8g^4}{x^4} + \frac{0.45g^2 + 8.1g^4}{x^6} \\
\frac{P_4}{gx} \;&=\; 1 + \frac{0}{x^2} + \frac{-\frac{0.28}{g^2} - 3.1 - 9.5g^2 - 19g^4}{x^4} + \frac{0.45 - 2.7g^2 - 3.9g^4}{x^6} + \frac{0.27g^2 + 5.4g^4}{x^8}\,.
\end{aligned} \tag{A.5}$$

As mentioned in the main text, we confirmed that this is indeed the twist-four, spin-0 operator which is exchanged between stress tensor multiplets, by computing its OPE coefficient directly at weak coupling. For this we worked out the corresponding eigenstate of the 1-loop dilatation operator, using the Hamiltonian from [66] (eq. 3.6 therein). Including double-trace terms, there are four color-singlet operators involving 4 scalars and no derivatives,

$$\mathcal{O}_\Delta = A\tfrac{1}{N_c^2}\mathrm{Tr}\big[\phi^i\phi^i\phi^j\phi^j\big] + B\tfrac{1}{N_c^2}\mathrm{Tr}\big[\phi^i\phi^j\phi^i\phi^j\big] + C\tfrac{1}{N_c^3}\mathrm{Tr}\big[\phi^i\phi^i\big]\big[\phi^j\phi^j\big] + D\tfrac{1}{N_c^3}\mathrm{Tr}\big[\phi^i\phi^j\big]\big[\phi^i\phi^j\big], \tag{A.6}$$

and we find that the eigenfunction corresponding to $\Delta = 4 + g^2(13 - \sqrt{41}) + O(g^4)$ is

$$(A, B, C, D) \propto \left(\sqrt{41} - 5,\ 4,\ \tfrac{1}{2}(35 - 5\sqrt{41}),\ -\sqrt{41} - 9\right) + O(g^2, 1/N_c^2). \tag{A.7}$$

By normalizing the two-point function of $\mathcal{O}_\Delta$ and computing its Wick contractions with two protected operators $\mathcal{O}(x_1, y_1)\mathcal{O}(x_2, y_2)$ of the form (2.1), we obtained the tree-level OPE coefficients (2.36). It was crucial in this calculation to retain the double-trace terms, which do contribute to the planar OPE coefficient. These are extremal three-point functions in the free-theory (the sum of twists of two operators is equal to the twist of the third operator) which are not predicted by the tree-level hexagon formulas [67, 68].

B Projection Functionals

In this appendix we detail the construction of projection functionals, which diagonalize the action of the B_v (or $\widehat{B}_{\mathrm{t}}$) on twist-two operators. The idea is exploit orthogonality relations for the polynomials which control their action on twist-two operators.

B.1 Action of $\widehat{B}_{\mathrm{t}}$ on operators near twist two

When acting on an operator with twist close to two, the functional of can be expanded as

$$\tfrac{1}{2} \lim_{\tau \to 2} \widehat{B}_{\mathrm{t}}[\ell, \ell + \tau] = a_\ell(\mathrm{t}) + (\tau - 2) b_\ell(\mathrm{t}) + O((\tau - 2)^2). \tag{B.1}$$

The factor $\frac{1}{2}$ is included for compatibility with the literature. The two shown terms are insensitive to descendants, thanks to the double-zeros of $\widehat{B}_{\mathrm{t}}$, which suppress operators of twists 4,6.... Thus, the Mellin representation (3.11) simplifies to

$$\lim_{\tau \to 2} \widehat{B}_{\mathrm{t}}[\ell, \ell + \tau] = \lim_{\tau \to 2} \frac{2\tau + 2 - \mathrm{t}}{\mathrm{t} - 6} \mathcal{Q}^0_{J+\tau+4, J}(10 - \mathrm{t}) + O((\tau - 2)^2)\,. \tag{B.2}$$

Comparing, one thus finds $a_\ell(\mathrm{t})$ in terms of the Mack polynomial (C.10), explictly

$$a_\ell(\mathrm{t}) = \frac{\Gamma(2\ell + 6)}{\Gamma(3)^2 \Gamma(\ell + 3)^2}\, {}_3F_2\left(-\ell, \ell + 5, \tfrac{\mathrm{t}-2}{2}; 3, 3; 1\right). \tag{B.3}$$

These polynomials are even under $\mathrm{t} \mapsto 10 - \mathrm{t}$, and are normalized so they obey the following orthogonality relation for $\ell \geq 0$:

$$c_\ell \int \frac{d\mathrm{t}}{4\pi i} \Gamma\left(4 - \tfrac{\mathrm{t}}{2}\right)^2 \Gamma\left(\tfrac{\mathrm{t}}{2} - 1\right)^2 a_\ell(\mathrm{t}) a_{\ell'}(\mathrm{t}) = \delta_{\ell, \ell'}, \tag{B.4}$$

where

$$c_\ell = \frac{\Gamma(\ell + 3)^4}{\Gamma(2\ell + 6)^2} (\ell + 1)_4 (2\ell + 5)\,. \tag{B.5}$$

These properties are similar to those of the leading-twist functional $B_{2,\mathrm{t}}$ discussed in section 4 of [39], although the details differ slightly since here we are interested in diagonalizing the action on twist-two operators, rather than on the leading double-twists.[9]

[9] The definition of a_ℓ and c_ℓ here coincides with the $\Delta_\phi = 3$ case of [39].

The slope $b_\ell(\mathrm{t})$ is more complicated. For our applications below, it will be useful to know its integrals against a_j. To this aim, we decompose it into odd and even parts. The odd part can be computed directly using symmetries of (B.2), while for the even part we adopt an expansion over Mack polynomials:

$$b_\ell(\mathrm{t}) - b_\ell(10-\mathrm{t}) = -g(\mathrm{t})^{-1}\frac{d}{d\mathrm{t}}\Big[a_\ell(\mathrm{t})g(\mathrm{t})\Big], \qquad g(\mathrm{t}) \equiv (-6+\mathrm{t})^2(-4+\mathrm{t})^2, \tag{B.6}$$

$$b_\ell(\mathrm{t}) + b_\ell(10-\mathrm{t}) = b_{\ell,-2}a_{-2}(\mathrm{t}) + \sum_{j\in 2\mathbb{N}}^{\ell} b_{\ell,j}a_j(\mathrm{t}). \tag{B.7}$$

In the second term we included a $j=-2$ term to account for the polar part of b_ℓ:

$$a_{-2}(\mathrm{t}) = \frac{2}{(-6+\mathrm{t})(-4+\mathrm{t})}\,. \tag{B.8}$$

From investigation of many cases, we find explicitly the coefficients

$$b_{\ell,-2} = \frac{-2\Gamma(2\ell+6)}{\Gamma(\ell+3)^2(\ell+1)(\ell+4)}, \tag{B.9}$$

$$b_{\ell,j} = \left(\frac{(\ell+2)^2(\ell+3)^2}{(j+2)(j+3)} - \frac{(\ell+1)^2(\ell+4)^2}{(j+1)(j+4)}\right)\frac{1}{(\ell-j)(\ell+j+5)}\frac{\Gamma(j+3)^2\Gamma(2\ell+6)(j+1)_4}{\Gamma(\ell+3)^2\Gamma(2j+5)(\ell+1)_4}, \tag{B.10}$$

$$b_{\ell,\ell} = 4H_{2\ell+4} - 6H_{\ell+2} - 2\frac{23+17\ell+3\ell^2}{(3+\ell)(4+\ell)(5+2\ell)}, \tag{B.11}$$

where the second line is for the generic case $0 \le j < \ell$. The factor outside the parenthesis matches the unsubtracted dispersion relation (4.45) of [39]) evaluated at $\Delta_\phi = 3$.

This representation enables us to find simply the integral of $b_\ell(\mathrm{t})$ against an even-spin a_j. The slight subtlety is that is that the non-polynomial function $a_{-2}(\mathrm{t})$ is not orthogonal to the polynomial ones, rather:

$$\int \frac{d\mathrm{t}}{4\pi i}\Gamma\big(4-\tfrac{\mathrm{t}}{2}\big)^2\Gamma\big(\tfrac{\mathrm{t}}{2}-1\big)^2 a_{-2}(\mathrm{t})a_j(\mathrm{t}) = \frac{-\Gamma(2j+6)}{\Gamma(j+3)^2(j+1)_4} \qquad (\ell \ge 0 \text{ even})\,. \tag{B.12}$$

Combining this with the orthogonality relation (B.4) and expansion (B.7), we find nice cancellations such that for even j, the integral of a Mack polynomial a_ℓ against b_j gives

$$I_{\ell,j} \equiv \int \frac{d\mathrm{t}}{4\pi i}\Gamma\big(4-\tfrac{\mathrm{t}}{2}\big)^2\Gamma\big(\tfrac{\mathrm{t}}{2}-1\big)^2 c_\ell a_\ell(\mathrm{t})b_j(\mathrm{t}) \tag{B.13}$$

$$= \begin{cases} \frac{1}{(j-\ell)(\ell+j+5)}\frac{(\ell+2)_2}{(j+2)_2}\frac{\Gamma(2j+6)\Gamma(\ell+3)^2}{\Gamma(2\ell+5)\Gamma(j+3)^2}, & \text{for } 0 \le \ell < j \text{ even}, \\ 2H_{2\ell+4} - 3H_{\ell+2} + \frac{13+8\ell+\ell^2}{(\ell+1)(\ell+3)(2\ell+5)}, & \text{for } \ell = j, \\ \frac{1}{(j+1)(j+4)}\frac{\Gamma(2j+6)\Gamma(\ell+3)^2}{\Gamma(2\ell+5)\Gamma(j+3)^2}, & \text{for } \ell > j \text{ even}. \end{cases} \tag{B.14}$$

This result, together with (B.7), will now be used to define various projectors; we will not further need the $b_{\ell,j}$ coefficients.

B.2 One-loop anomalous dimensions: the $\Phi_{\ell,\ell+2}$ projection functionals

In [39] a functional Φ_ℓ was constructed analytically, which had double-zeros on all operators of the first double-twist family of an arbitrary CFT, and single zeros on just the $J=\ell$ one. The sign properties of that functional, for some ℓ and external operator dimensions, established that mean field theory maximizes the twist gap for that spin.

Here we will construct functionals Φ_{ℓ_1,ℓ_2} which analogously has double-zeros near twist $\tau=2$, except for two operators $J=\ell_1,\ell_2$, where it has a single zero. This problem is similar, but distinct, from the one studied in [39] since here we insist to maintain double-zeros on every double-twist $\tau\geq 4$.

As a first step, we attempt to construct a functional Φ_ℓ with nonvanishing slope only for $J=\ell$, by writing it as an integral over $\widehat{B}_{\mathrm{t}}$:

$$\Phi_\ell[\Delta,J]\equiv\int\frac{d\mathrm{t}}{4\pi i}\Phi_\ell[\mathrm{t}]\ \widehat{B}_{\mathrm{t}}[\Delta,J]. \tag{B.15}$$

We will find that the kernel $\Phi_\ell[\mathrm{t}]$ does not lead to a convergent integral unless we allow a nonvanishing slope on at least two spins. The construction follows that in [39], although Φ_ℓ here is slightly different. The conditions on Φ_ℓ are that, for every even $J\geq 0$,

$$\int\frac{d\mathrm{t}}{2\pi i}\Phi_\ell[\mathrm{t}]a_J(\mathrm{t})=0,\qquad \int\frac{d\mathrm{t}}{2\pi i}\Phi_\ell[\mathrm{t}]b_J(\mathrm{t})\stackrel{?}{=}\delta_{\ell,J}\,. \tag{B.16}$$

Note that a factor 2 arose from (B.1). The question mark emphasizes that Φ_ℓ will be obtained by ignoring convergence constraints, which will be addressed below.

First, we observe that first of eqs. (B.16) can be satisfied if the kernel is odd: $\Phi_\ell[10-\mathrm{t}]=-\Phi_\ell[\mathrm{t}]$. Since the a_J's form a complete basis for a reasonable function space, we expect this to be the only solution. For an odd kernel, the second condition, about the slope, can be computed from (B.6) as

$$\int\frac{d\mathrm{t}}{2\pi i}\Phi_\ell[\mathrm{t}]b_J(\mathrm{t})=-\frac{1}{2}\int\frac{d\mathrm{t}}{2\pi i}\Phi_\ell[\mathrm{t}]g(\mathrm{t})^{-1}\frac{d}{d\mathrm{t}}\Big[a_J(\mathrm{t})g(\mathrm{t})\Big]\,. \tag{B.17}$$

Assuming that $\Phi_\ell[\mathrm{t}]$ vanishes at infinity faster than any polynomial (otherwise the functional (B.15) doesn't make much sense), we integrate by parts to write the second condition as

$$\delta_{\ell,J}=\frac{1}{2}\int\frac{d\mathrm{t}}{2\pi i}\left(g(\mathrm{t})\frac{d}{d\mathrm{t}}\big[\Phi_\ell[\mathrm{t}]g(\mathrm{t})^{-1}\big]\right)a_J(\mathrm{t})\,. \tag{B.18}$$

Comparing with the orthogonality relation (B.4), we deduce that the parenthesis should be proportional to $c_\ell a_\ell(\mathrm{t})$, specifically

$$g(\mathrm{t})\frac{d}{d\mathrm{t}}\big[\Phi_\ell[\mathrm{t}]g(\mathrm{t})^{-1}\big]=\Gamma\big(4-\tfrac{\mathrm{t}}{2}\big)^2\,\Gamma\big(\tfrac{\mathrm{t}}{2}-1\big)^2\,c_\ell a_\ell(\mathrm{t})\,. \tag{B.19}$$

This differential equation admits a unique solution, given that $\Phi_\ell[\mathrm{t}]$ is odd and so must vanish at $\mathrm{t}=5$:

$$\Phi_\ell[\mathrm{t}] = g(\mathrm{t})\int_5^{\mathrm{t}} d\mathrm{t}'\frac{c_\ell a_\ell(\mathrm{t}')}{g(\mathrm{t}')}\Gamma\left(4-\tfrac{\mathrm{t}'}{2}\right)^2\Gamma\left(\tfrac{\mathrm{t}'}{2}-1\right)^2 \tag{B.20}$$

$$= \frac{i\pi^2}{16}(y^2+1)^2\int_0^y \frac{dy'\; c_\ell a_\ell(5+iy')}{\cosh(\frac{\pi y'}{2})^2} \tag{B.21}$$

where we let $\mathrm{t}=5+iy$ in the second line. The first few cases can be found analytically, for example

$$\Phi_0[5+iy] = i\frac{\pi}{8}(1+y^2)^2\tanh(\tfrac{\pi y}{2}), \tag{B.22}$$

$$\Phi_2[5+iy] = i\frac{(1+y^2)^2}{448\pi}\Big(28\left(\pi y\log(1+e^{-\pi y})-\mathrm{Li}_2(-e^{-\pi y})+\tfrac{\pi^2}{12}(3y^2-1)\right)+\pi^2(9-7y^2)\tanh(\tfrac{\pi y}{2})\Big), \tag{B.23}$$

which are indeed odd functions of y. The only issue with this calculation is that the Φ_ℓ kernels don't actually vanish as $y\to\infty$: the corresponding functionals do not make sense as the integral (B.15) fails to converge at large y. The solution is to take finite linear combinations. By investigating the large-t limit of the kernels we find the following simple formula:

$$\lim_{t\to 5+i\infty}\frac{\Phi_\ell[\mathrm{t}]}{i\pi g(\mathrm{t})} \equiv \Phi_\ell^\infty = \frac{\Gamma(\ell+3)^2}{2\Gamma(2\ell+5)}H_{\ell+2}. \tag{B.24}$$

Since the integrand in (B.21) decays exponentially, the corrections to the limit are proportional to $e^{-\pi y}$. Thus, to define valid functionals, it suffices to combine any two kernels $\Phi_\ell[\mathrm{t}]$ so as to cancel the constant:

$$\Phi_{\ell_1,\ell_2}[\mathrm{t}] \equiv \Phi_{\ell_1}[\mathrm{t}] - \frac{\Phi_{\ell_1}^\infty}{\Phi_{\ell_2}^\infty}\Phi_{\ell_2}[\mathrm{t}]\,. \tag{B.25}$$

We have normalized it so it has unit slope as $\tau\to 2$ when acting on operators of spin $J=\ell_1$. The Φ_{ℓ_1,ℓ_2} are of course not all linearly independent, they are spanned by the $\Phi_{\ell,\ell+2}$ considered in the main text. A convenient formula for their evaluation is discussed in B.4 below.

As discussed in the main text below (3.24), the combination (B.25) admits a simple interpretation in terms of one-loop anomalous dimensions, since the one-loop sum rule forces the following proportionality (with an ℓ-independent constant):

$$\Phi_\ell^\infty \propto C_\ell^{(0)}\gamma_\ell^{(1)}\,. \tag{B.26}$$

This is indeed satisfied by (B.24). In other words, the Φ_{ℓ_1,ℓ_2} sum rules analytically prove the one-loop formula for anomalous dimensions. This also makes it physically clear why a functional with a single zero on only one spin could not exist, since that would prove that one-loop anomalous dimensions identically vanish.

B.3 One-loop OPE coefficients: the Ψ_ℓ functionals

The functionals just constructed possess desirable zero structure which makes them highly particularly sensitive to the scaling dimension of leading-twist operators of a given spin. However, they lack sensitivity to OPE coefficients, which are the main focus of this paper.

We now construct, for each even $\ell \geq 0$, a functional Ψ_ℓ which has double zeros around twist two for all spins except $J = \ell$, where it has nonvanishing constant term *and* slope. At weak coupling, Ψ_ℓ effectively relates the OPE coefficient and scaling dimension of the leading spin-ℓ operator. In terms of a kernel $\Psi_\ell[\mathrm{t}]$ defined similarly to (B.15), these conditions are interpreted as follows:

$$\int \frac{d\mathrm{t}}{2\pi i}\Psi_\ell[\mathrm{t}]a_J(\mathrm{t}) = \delta_{\ell,J}, \tag{B.27}$$

$$\int \frac{d\mathrm{t}}{2\pi i}\Psi_\ell[\mathrm{t}]b_J(\mathrm{t}) = \delta_{\ell,J}\beta_\ell, \tag{B.28}$$

for all even $J \geq 0$, and where β_ℓ is an a-priori unknown constant.

To construct the kernel $\Psi_\ell[\mathrm{t}]$, we propose to make an ansatz as a sum of its even and odd parts. The orthogonality relation (B.4) immediately fixes the even part:

$$\begin{aligned}\Psi_\ell[\mathrm{t}] &\equiv \Psi_\ell^{\mathrm{E}}[\mathrm{t}] + \Psi_\ell^{\mathrm{O}}[\mathrm{t}],\\ \Psi_\ell^{\mathrm{E}}[\mathrm{t}] &= \frac{1}{2}\Gamma\Big(4-\tfrac{\mathrm{t}'}{2}\Big)^2\Gamma\Big(\tfrac{\mathrm{t}'}{2}-1\Big)^2 c_\ell a_\ell(\mathrm{t})\,,\end{aligned} \tag{B.29}$$

where the odd part satisfies $\Psi_\ell^{\mathrm{O}}[10-\mathrm{t}] = -\Psi_\ell^{\mathrm{O}}[\mathrm{t}]$. This takes care of (B.27).

We now substitute the ansatz into the second condition (B.28) and evaluate the even contribution using the integral $I_{\ell,J}$ in (B.13):

$$I_{\ell,J} + \int \frac{d\mathrm{t}}{2\pi i}\Psi_\ell^{\mathrm{O}}[\mathrm{t}]b_J(\mathrm{t}) = \delta_{\ell,J}\beta_\ell \qquad \text{(for all even } J \geq 0\text{)}. \tag{B.30}$$

Since we formally diagonalized the b_J integral using the kernel $\Phi_J[\mathrm{t}]$ (see (B.16)), this system can be inverted as an infinite sum

$$\Psi_\ell^{\mathrm{O}}[\mathrm{t}] \equiv \Phi_\ell[\mathrm{t}]\beta_\ell - \sum_{n=0}^{\infty} I_{\ell,2n}\Phi_{2n}[\mathrm{t}]\,. \tag{B.31}$$

The single parameter left to determine is β_ℓ. As above, it is fixed by the requirement that the kernel must vanish at large t for the functional to make sense, which gives

$$0 = \beta_\ell\Phi_\ell^\infty - \sum_{n=0}^{\infty} I_{\ell,2n}\Phi_{2n}^\infty \tag{B.32}$$

$$\Rightarrow \quad \beta_\ell H_{\ell+2} = I_{\ell,\ell} + \sum_{n=0}^{\frac{\ell}{2}-1}\frac{(4n+5)H_{2n+2}}{(2n+1)(2n+4)} + \sum_{n=1}^{\infty}\frac{(\ell+2)_2(2\ell+5+4n)H_{\ell+2+2n}}{2n(\ell+2+2n)_2(2\ell+5+2n)}\,, \tag{B.33}$$

where we plugged in the explicit limit (B.24). Perhaps surprisingly, these sum up to simple rational numbers. In fact, as discussed below (3.25) in the main text, there is a simple analytic guess for the result, which is required for the sum rule to be satisfied at one-loop:

$$\beta_\ell = H_{2\ell+4} - H_{\ell+2} + \frac{S_2(\ell+2)}{2H_{\ell+2}}\,. \tag{B.34}$$

We verified numerically that this agrees precisely with (B.33) for many values of ℓ.

To summarize starting from (B.29), the action of the Ψ_ℓ functional is computed is

$$\Psi_\ell[\Delta, J] = \int \frac{d\mathrm{t}}{4\pi i}\Psi_\ell[\mathrm{t}]\widehat{B}_\mathrm{t}[\Delta, J], \tag{B.35}$$

with the kernel defined by

$$\Psi_\ell[\mathrm{t}] = \frac{1}{2}\Gamma\Big(4-\tfrac{\mathrm{t}'}{2}\Big)^2\,\Gamma\Big(\tfrac{\mathrm{t}'}{2}-1\Big)^2\,c_\ell a_\ell(\mathrm{t}) + \beta_\ell\Phi_\ell[\mathrm{t}] - \sum_{n=0}^{\infty} I_{\ell,2n}\Phi_{2n}[\mathrm{t}]\,. \tag{B.36}$$

The functions $\Phi_\ell[\mathrm{t}]$ are defined in (B.21) and the coefficients $I_{\ell,2n}$ and β_ℓ can be found in (B.13) and (B.34) respectively.

B.4 Formulas for evaluating Φ and Ψ functionals

We now describe a practical way to perform the t integral that define the projection functionals, starting with Φ_{ℓ_1,ℓ_2} in (B.15), when acting on a generic state. Following the method in section C.3, it suffices to evaluate the following basic integrals for integer $k \geq 0$:

$$[\Phi_{\ell_1,\ell_2}]_k \equiv \int \frac{d\mathrm{t}}{4\pi i}\Phi_{\ell_1,\ell_2}[\mathrm{t}]\frac{(\frac{\mathrm{t}-2}{2})_k}{\mathrm{t}-6}\,. \tag{B.37}$$

Indeed it is clear from the definition of $\widehat{B}_\mathrm{t}$ that the action of Φ_{ℓ_1,ℓ_2} on any state can be written as a finite sum of these integrals (see (3.11)). When plugging in the integral representation (B.21), the $1/(\mathrm{t}-6)$ denominator neatly cancels out:

$$[\Phi_{\ell_1,\ell_2}]_k = \frac{1}{8i}\int_{-\infty}^{\infty}\frac{dy}{4\pi}(1+y^2)(\tfrac{1+iy}{2})_{k+1}\int_0^y \frac{\pi^2 dy'}{\cosh(\frac{\pi y}{2})^2}\left[c_{\ell_1}a_{\ell_1}(5+iy') - \frac{\Phi^\infty_{\ell_1}}{\Phi^\infty_{\ell_2}}c_{\ell_2}a_{\ell_2}(5+iy')\right]. \tag{B.38}$$

Again we have set $\mathrm{t} = 5+iy$. This looks daunting, but the trick is to integrate by parts, using that the inner integral vanishes exponentially at infinity. This yields a difference of two integrals,

$$[\Phi_{\ell_1,\ell_2}]_k = [\Phi_{\ell_1}]_k - \frac{\Phi^\infty_{\ell_1}}{\Phi^\infty_{\ell_2}}[\Phi_{\ell_2}]_k\,, \tag{B.39}$$

where

$$[\Phi_\ell]_k \equiv \frac{1}{16i}\int_{-\infty}^{\infty}\frac{\pi^2 dy}{4\pi\cosh(\frac{\pi y}{2})^2}c_\ell a_\ell(5+iy)\int_i^y dy'(1+y'^2)\left[(\tfrac{1+iy'}{2})_{k+1} - (\tfrac{1-iy'}{2})_{k+1}\right]. \tag{B.40}$$

Note that we antisymmetrized in y', which was not strictly necessary but makes each $[\Phi_\ell]_k$ real. The calculation is thus reduced to integrating a polynomial divided by $\cosh^2$. This can be completed term-by-term using the identity

$$\int_{-\infty}^{\infty} \frac{dy}{4\pi} \frac{\pi^2}{\cosh^2(\pi y/2)} y^q = (-1)^{1+q/2}(2^q-2)B_q, \tag{B.41}$$

where B_q on the right is the Bernouilli number, not to be confused with the position-space functional B_v. In this way $[\Phi_\ell]_k$ can be evaluated as an exact rational number.

The y' lower bound in (B.40) is arbitrary since any constant added to the integral would cancel out in the combination (B.39), thanks to the definition of Φ_ℓ^∞. The choice made above, which makes the integral proportional to $(1+y^2)$, turns out to ensure that $[\Phi_\ell]_k = 0$ for $\ell > k$, which will be convenient below. This can be interpreted as an orthogonality property of the Mack polynomials, although we were not able to strictly derive it from (B.4). Example values of $[\Phi_\ell]_k$ and $[\Phi_{0,2}]_k$ are given in table 4.

For the Ψ_ℓ functional (B.36), we follow the same strategy and integrate by parts in all the terms involving $\Phi_k[\mathrm{t}]$. The even contribution is simpler and we could in fact do it analytically; we record only the result,

$$\begin{aligned}[\Psi_\ell]_k \equiv \int \frac{d\mathrm{t}}{4\pi i} \Psi_\ell[\mathrm{t}] \frac{(\frac{\mathrm{t}-2}{2})_k}{\mathrm{t}-6} = \frac{\Gamma(\ell+3)^2\Gamma(k+2)}{4\Gamma(2\ell+5)} \left[\frac{(k-\ell)_{\ell+3}}{(k+1)_{\ell+4}}(k+7+\ell(\ell+5))-1\right] \\ + \beta_\ell [\Phi_\ell]_k - \sum_{n=0}^{\lfloor k/2 \rfloor} I_{\ell,2n} [\Phi_{2n}]_k \ .\end{aligned} \tag{B.42}$$

The crucial fact is that that the n sum terminates, thanks to the vanishing properties just mentioned. Thus, while we were unable to find a closed-form expression for the kernel $\Psi_\ell[\mathrm{t}]$ itself, it is possible to compute its action on a state of arbitrary spin J as a *finite* sum of $\sim J$ terms. The sum gives rational numbers exemplified in table 4. We have verified that they agree with the direct numerical integration of (B.35), with the sum over n truncated to a large order.

B.5 Sign properties of Φ and Ψ functionals

The formulas from the preceding section, combined with the Mack polynomials reviewed in section C.2, enable to rapidly compute the $\Phi_{\ell,\ell+2}$ and Ψ functionals on generic states. One readily sees from figure 14 that $\Phi_{0,2}$ indeed has the claimed single zeros at spins 0 and 2 and twist 2, and double zeros on higher spins and all higher twists. However, since the slopes on spin 0 and 2 have opposite signs, it is not sign definite as also visible from the figure. In fact, for $J > 0$ the $\Phi_{0,2}$ functional is negative for $\tau < \tau^*$ and eventually becomes positive at large enough twist τ.

Similarly, we show the action of Ψ_0 in fig. 15, which features double-zeros on all double-twists for $J \geq 2$ and it is non-zero when acting on the Konishi operator. Remarkably, we find that the functional is nonnegative for all $\tau \geq 2$. The same property is actually shared by all the Ψ_ℓ: we observe that $\Psi_\ell[\Delta, J]$ identically vanishes for $J < \ell$ and is positive otherwise.

k	0	1	2	3	4	5	6	7
$[\Phi_0]_k$	$-\frac{1}{30}$	$-\frac{1}{15}$	$-\frac{59}{315}$	$-\frac{44}{63}$	$-\frac{1031}{315}$	$-\frac{278}{15}$	$-\frac{20332}{165}$	$-\frac{31072}{33}$
$[\Phi_2]_k$	0	0	$-\frac{2}{735}$	$-\frac{16}{735}$	$-\frac{1228}{8085}$	$-\frac{424}{385}$	$-\frac{19696}{2275}$	$-\frac{1866112}{25025}$
$[\Phi_4]_k$	0	0	0	0	$-\frac{5}{11011}$	$-\frac{90}{11011}$	$-\frac{108}{1001}$	$-\frac{14496}{11011}$
$[\Phi_{0,2}]_k$	$-\frac{1}{30}$	$-\frac{1}{15}$	$-\frac{37}{225}$	$-\frac{116}{225}$	$-\frac{4943}{2475}$	$-\frac{7658}{825}$	$-\frac{2708092}{53625}$	$-\frac{1536544}{4875}$
$[\Psi_0]_k$	$-\frac{103}{1800}$	$-\frac{73}{900}$	$-\frac{5996}{33075}$	$-\frac{3722}{6615}$	$-\frac{74534}{33075}$	$-\frac{17492}{1575}$	$-\frac{496730}{7623}$	$-\frac{84661744}{190575}$

Table 4: Example results for the $[\Phi_\ell]_k$ integral in (B.40), and for two physical functionals derived from it.

C Formulas for efficient evaluation of functionals

The bootstrap method requires the evaluation of a large menu of trial functionals on a large sample of states (Δ, J). High accuracy is required, since optimal combinations tend to involve large numerical cancellations between different functionals. Here we detail fast and accurate numerical methods.

C.1 Dispersion relations in position space

The most straightforward method to compute the Polyakov-Regge block $\mathcal{P}_{\Delta,J}(u,v)$ is perhaps to compute the dispersive integral (2.17). The kernel is that of the unsubtracted dispersion relation of [42]; our conventions follow those in (2.9) of [39], where we combine the s and t-channels:

$$K(u,v;u',v') = \frac{u'-v'}{64\pi(uvu'v')^{\frac{3}{4}}} x^{\frac{3}{2}} {}_2F_1(\tfrac{1}{2},\tfrac{3}{2},2,1-x)\ \theta(\sqrt{v'}-(\sqrt{u}+\sqrt{v}+\sqrt{u'})) \\ + \frac{1}{4\pi(uvu'v')^{\frac{1}{4}}} \frac{\sqrt{u'}+\sqrt{v'}}{(\sqrt{u}+\sqrt{u'})(\sqrt{v}+\sqrt{u'})}\ \delta(\sqrt{v'}-(\sqrt{u}+\sqrt{v}+\sqrt{u'})), \quad \text{(C.1)}$$

where x is a remarkable combination of four cross-ratios:

$$x = \frac{16\sqrt{uvu'v'}}{\left[(\sqrt{u}+\sqrt{v})^2-(\sqrt{u'}+\sqrt{v'})^2\right]\left[(\sqrt{u}-\sqrt{v})^2-(\sqrt{u'}-\sqrt{v'})^2\right]}\,. \quad \text{(C.2)}$$

In practice, we perform the double integral in (2.16) by changing to ρ coordinates, in which the kernel also takes a concise form. By adapting the radial coordinates from [69] to the u-channel, we obtain

$$\rho = \frac{1}{(\sqrt{1-w}+\sqrt{-w})^2}, \qquad \overline{\rho} = \frac{1}{(\sqrt{1-\overline{w}}+\sqrt{-\overline{w}})^2}. \quad \text{(C.3)}$$

The choice of numerical integration strategy matters. In `Mathematica`, we force the use of the `DoubleExponential` method, which essentially computes a simple Riemann sum after a

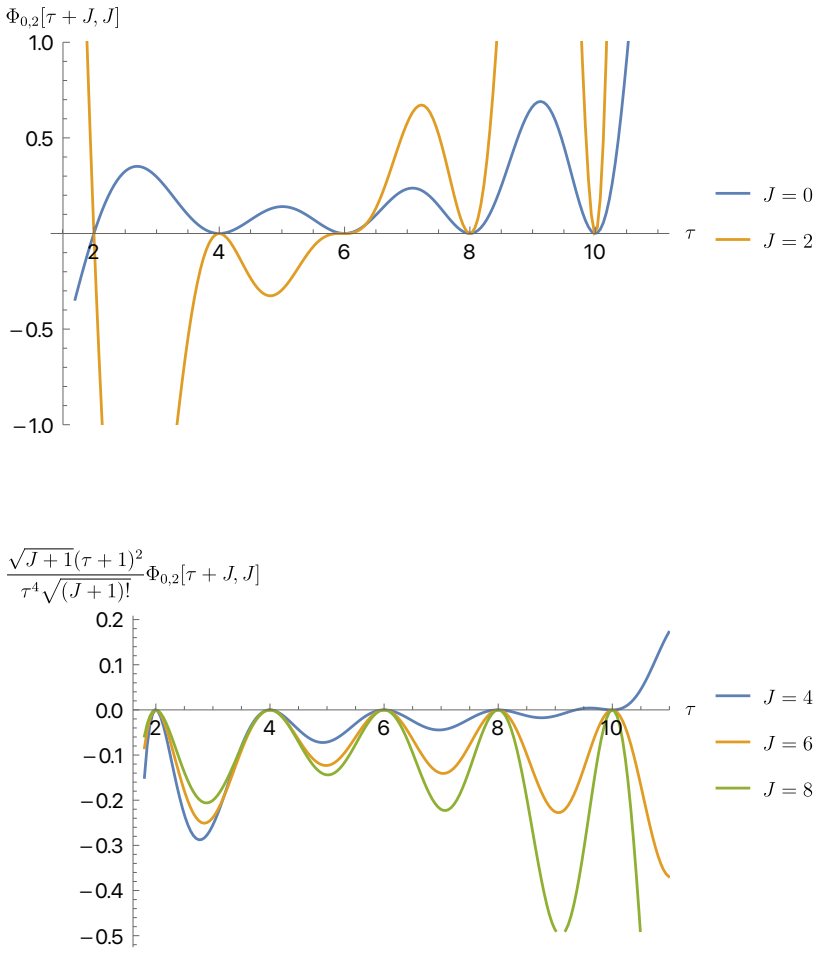

Figure 14: Action of the $\Phi_{0,2}$ functional. We plot the action of $\Phi_{0,2}$ for spins $J = 0, 2$ in the first panel, and the rescaled functional $\frac{\sqrt{J+1}(\tau+1)^2}{\tau^4\sqrt{(J+1)!}}\Phi_{0,2}$ for larger spin in the second one for visual clarity. For $J > 0$, the functionals are initially negative for $\tau > 2$, but they become positive at large enough twist.

clever change of variable that makes the integrand decay exponentially near its endpoints. In theory, for a sufficiently "nice" integrand, the error with this method decreases exponentially with effort, however we only observe a decrease in error if we also force subdivisions using the `MinRecursion` option. For example, the two-dimensional ρ integral with

```
NIntegrate[..., Method -> {"DoubleExponential", "SymbolicProcessing" -> 0},
                MinRecursion -> 2, WorkingPrecision -> 25]
```

will typically achieve near 20 digits of accuracy, which generally suffices for bootstrap problems

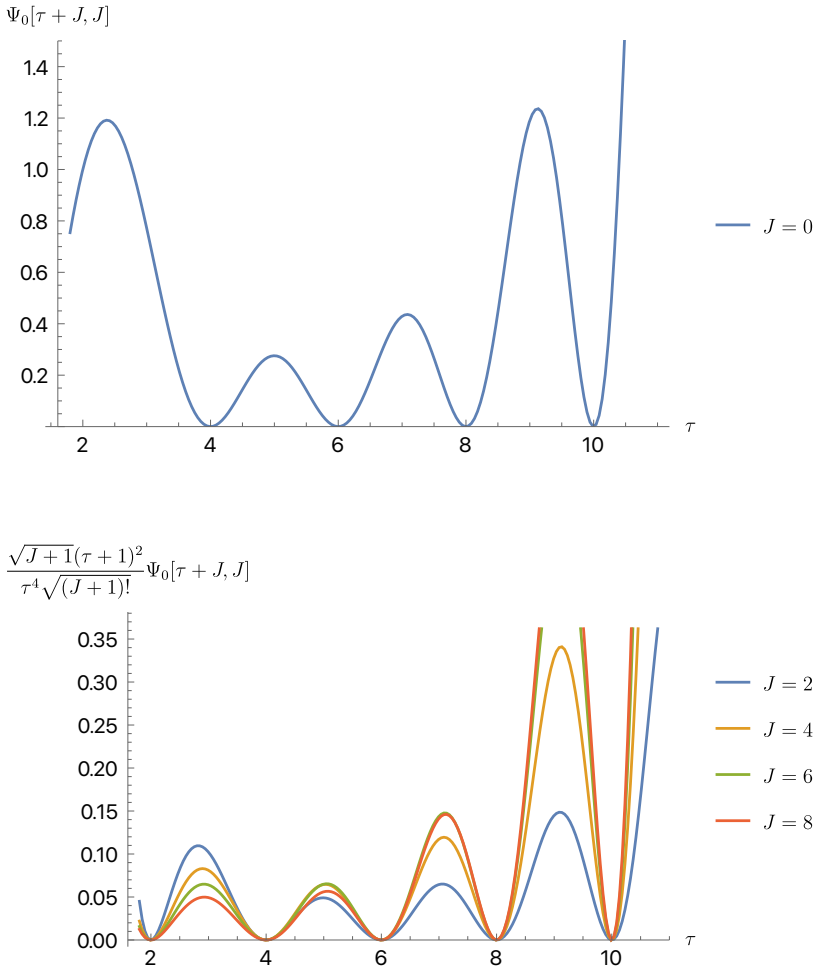

Figure 15: Action of the functionals at low twist. We plot Ψ_0 in the first panel for $J = 0$, and $\frac{\sqrt{J+1}(\tau+1)^2}{\tau^4\sqrt{(J+1)!}}\Psi_0$ in the second panel for visual clarity. This functional is positive-definite for all spin and all twist $\tau \geq 2$.

with $O(30)$ functionals or fewer. One way to estimate accuracy is to make simple changes of variable such as $\rho_w \mapsto \rho_w^2$, which theoretically should not change the integral but in practice do so with this method. We observe that each increase in MinRecursion typically adds about 10 significant figures at the cost of quadrupling the computation time. Therefore, arbitrary accuracy is in principle achievable with this method, but only for a limited number of functionals/states.

C.2 Mack polynomials

In this appendix we detail our evaluation of formulas involving the Mellin representation and Mack polynomials. For future reference, we keep explicit the dependence on external operator dimensions $\{\Delta_i\} = \{\Delta_1, \Delta_2, \Delta_3, \Delta_4\}$ and spacetime dimension d; only the case $\{\Delta_i\} = \{4, 4, 4, 4\}$ and $d = 4$ is relevant for the main text.

To fix our conventions, we use the following Mellin representation for unequal operators following the convention of [41]:

$$\langle \mathcal{O}(x_1)\cdots\mathcal{O}(x_4)\rangle = \frac{1}{(x_{13}^2)^{\frac{\Delta_1+\Delta_2+\Delta_3-\Delta_4}{2}}(x_{24}^2)^{\Delta_2}}\frac{(x_{34}^2)^{\frac{\Delta_1+\Delta_2-\Delta_3-\Delta_4}{2}}}{(x_{14}^2)^{\frac{\Delta_1+\Delta_4-\Delta_2-\Delta_3}{2}}}\mathcal{G}(u,v), \tag{C.4}$$

$$\begin{aligned}\mathcal{G}(u,v) = \iint_{\gamma_C}\frac{ds dt}{(4\pi i)^2}&\Gamma(\tfrac{\Delta_1+\Delta_2-s}{2})\Gamma(\tfrac{\Delta_3+\Delta_4-s}{2})\Gamma(\tfrac{\Delta_2+\Delta_3-t}{2})\Gamma(\tfrac{\Delta_1+\Delta_4-t}{2})\\ &\times\Gamma(\tfrac{\Delta_2+\Delta_4-u}{2})\Gamma(\tfrac{\Delta_1+\Delta_3-u}{2})u^{\frac{s-\Delta_1-\Delta_2}{2}}v^{\frac{t-\Delta_2-\Delta_3}{2}}M_{s,t}\end{aligned} \tag{C.5}$$

where $s+t+u = \sum_{i=1}^4\Delta_i$, and the contour γ_C is determined by the Gamma functions. Then the Mack polynomial $\mathcal{Q}_{\Delta,J}^{m,\{\Delta_i\}}(t)$ is the residue at $s = \Delta - J + 2m$ in the Mellin representation of a conformal block $G_{\Delta,J}(u,v)$ (or Polyakov-Regge block, which differs by double-twist contributions).

For our applications below, it is useful to explicit the m and t dependence of the Mack polynomials. Up to overall Γ-functions, the dependence is essentially through a polynomial of total degree J which is naturally written using Pochhammer symbols [38, 70]:

$$\mathcal{Q}_{\Delta,J}^{m,\{\Delta_i\}}(t) = K_{\Delta,j}^{m,\{\Delta_i\}}Q_{\Delta,J}^{m,a,b}(t-\Delta_2-\Delta_3),\quad Q_{\Delta,J}^{m,a,b}(t') \equiv \sum_{q=0}^{J}\sum_{k=0}^{J-q}(-m)_q\left[Q_{\Delta,J}^{a,b}\right]_{q,k}\left(-\tfrac{t'}{2}\right)_k. \tag{C.6}$$

Here and below $a = \frac{\Delta_2-\Delta_1}{2}$, $b = \frac{\Delta_3-\Delta_4}{2}$. The prefactor, which contains the double-twist zeros mentioned in the main text, is

$$\begin{aligned}K_{\Delta,J}^{m,\{\Delta_i\}} =& \frac{1}{m!(\Delta-\frac{d}{2}+1)_m\Gamma(\Delta-1)\Gamma\left(\frac{\Delta_1+\Delta_2-\Delta+J}{2}-m\right)\Gamma\left(\frac{\Delta_3+\Delta_4-\Delta+J}{2}-m\right)}\\ &\times\frac{2\Gamma(\Delta+J)\Gamma(\Delta+J-1)}{\Gamma\left(\frac{\Delta+J+\Delta_1-\Delta_2}{2}\right)\Gamma\left(\frac{\Delta+J+\Delta_2-\Delta_1}{2}\right)\Gamma\left(\frac{\Delta+J+\Delta_3-\Delta_4}{2}\right)\Gamma\left(\frac{\Delta+J+\Delta_4-\Delta_3}{2}\right)},\end{aligned} \tag{C.7}$$

whereas the coefficients $\left[Q_{\Delta,J}^{a,b}\right]_{q,k}$ are rational functions of Δ. It is useful to view them as a $(J+1)\times(J+1)$ matrix where q, k range from 0 to J, setting to zero the entries with $q+k > J$. The matrix can be populated efficiently using the Casimir recursion in appendix A of [9]. In

the Pochhammer basis, we find

$$\begin{aligned}
&\big((2q+k-J)(\Delta-J+1-d+q)-(J+k+d-2)(J-k-q)\big)\left[Q^{a,b}_{\Delta,J}\right]_{q,k}\\
&\quad=(k+1)(\tfrac{\Delta-J}{2}+a+q+k)(\tfrac{\Delta-J}{2}+b+q+k)\left[Q^{a,b}_{\Delta,J}\right]_{q,k+1}\\
&\qquad+(k+1)(J-2k-q-a-b+1-d/2)\left[Q^{a,b}_{\Delta,J}\right]_{q-1,k+1}\\
&\qquad-2(J+1-q-k)\left[Q^{a,b}_{\Delta,J}\right]_{q-1,k}\,.
\end{aligned}\tag{C.8}$$

This recursion is seeded with the boundary condition $\left[Q^{a,b}_{\Delta,J}\right]_{0,J}=(-1)^{J+1}$ for the top-right element, which corresponds to the conformal block normalization $\lim_{u\ll 1-v\ll 1}G_{\Delta,J}(u,v)=u^{\frac{\Delta-J-\Delta_1-\Delta_2}{2}}(1-v)^J$. We fill the matrix row-by-row using (C.8) to move leftward in k. For example, for the first row ($q=0$) one finds the simple analytic solution

$$\left[Q^{a,b}_{\Delta,J}\right]_{0,k}=\frac{(-1)^{J+1}J!(\Delta+J-1)_{k-J}}{k!(J-k)!\big(\frac{\Delta+J}{2}+a\big)_{k-J}\big(\frac{\Delta+J}{2}+b\big)_{k-J}},\tag{C.9}$$

which resums (see (C.6)) to give the standard $m=0$ Mack polynomial [9, 70]

$$Q^{0,a,b}_{\Delta,J}(\mathrm{t}')=(-1)^{J+1}\frac{\big(\frac{\Delta+J}{2}+a\big)_J\big(\frac{\Delta+J}{2}+b\big)_J}{(\Delta-1)_J}{}_3F_2\big(\{-J,\Delta-1,-\tfrac{\mathrm{t}'}{2}\},\{\tfrac{\Delta-J}{2}+a,\tfrac{\Delta-J}{2}+b\},1\big).\tag{C.10}$$

Populating the entire matrix $\left[Q^{a,b}_{\Delta,J}\right]_{q,k}$ requires only $O(J^2)$ multiplications. For $J\sim 100$ and rational values of Δ, this task can be completed with exact rational arithmetic in a fraction of a second, on a typical laptop.

A slightly upsetting feature of (C.8) is that it produces spurious poles at values of Δ that are not particularly meaningful, where the factor on the left-hand-side vanishes. We either avoid these values or fall back on the following analytic expression for the coefficients (see the formula recorded in appendix of [41]), which is explicitly free of spurious poles:

$$\begin{aligned}
\left[Q^{a,b}_{\Delta,J}\right]_{q,k}=&\frac{J!}{(J-k-q)!k!}\frac{(\frac{\Delta-J}{2}+b+k+q)_{J-k-q}}{(J-q+\frac{d}{2}-1)_q}\\
&\times\sum_{p=0}^{q}\frac{(-1)^{k+p}}{p!(q-p)!}\frac{(\frac{\Delta-J}{2}+a+k+q-p)_{J-k-q}}{(\Delta-J+2-d)_{q-p}(\Delta+k+q-p-1)_{J-k-q+p}}\\
&\times\big(\tfrac{\Delta-J-d+2}{2}-b\big)_{q-p}\big(\tfrac{\Delta-J-d+2}{2}+a\big)_{q-p}\big(\tfrac{\Delta+J}{2}-b-p\big)_p\big(\tfrac{\Delta+J}{2}+a-p\big)_p\,.
\end{aligned}\tag{C.11}$$

Populating the $\left[Q^{a,b}_{\Delta,J}\right]_{q,k}$ matrix with this formula requires $O(J^3)$ multiplications.

C.3 Formulas for B functionals using Mack polynomials

The representation (C.6) is convenient for our purposes because the m dependence is isolated in a few Pochhammer symbols. Consider for example the $\widehat{B}_{\mathrm{t}}$ functional, which we recall from

(3.11):

$$\widehat{B}_{\rm t}[\Delta,J]=\sum_{m=0}^{\infty}\frac{2(\Delta-J+2m)+2-t}{t-6}\mathcal{Q}^{m,\{4,4,4,4\}}_{\Delta+4,J}(10-{\rm t}). \tag{C.12}$$

The dependence on m is explicit in K and $(-m)_q$, which allows the sum over the infinite number of descendants to be performed analytically. The basic formula is

$$\sum_{m=0}^{\infty}K^{m,\{\Delta_i\}}_{\Delta,J}(-m)_q=\tilde{K}^{\{\Delta_i\}}_{\Delta,J}\frac{(\frac{\Delta-J-\Delta_1-\Delta_2+2}{2})_q(\frac{\Delta-J-\Delta_3-\Delta_4+2}{2})_q}{(\frac{d+4-\Delta_1-\Delta_2-\Delta_3-\Delta_4}{2}-J)_q}\,, \tag{C.13}$$

$$\tilde{K}^{\{\Delta_i\}}_{\Delta,J}\equiv K^{0,\{\Delta_i\}}_{\Delta,J}\times\frac{\Gamma\big(\Delta+1-\frac{d}{2}\big)\Gamma\big(\frac{\Delta_1+\Delta_2+\Delta_3+\Delta_4-d-2}{2}+J\big)}{\Gamma\big(\frac{\Delta+J+\Delta_1+\Delta_2-d}{2}\big)\Gamma\big(\frac{\Delta+J+\Delta_3+\Delta_4-d}{2}\big)}\,. \tag{C.14}$$

From here, we specialize to the $\Delta_i=4$ case of interest and abbreviate: $\tilde{K}^{N=4}_{\Delta,J}\equiv\tilde{K}^{\{4,4,4,4\}}_{\Delta+4,J}$. The nonnegative factor $\tilde{K}^{N=4}_{\Delta,J}$ will be present in front of most functionals.

Explicitly, we thus compute $\widehat{B}_{\rm t}$ in (3.11) by forming the vector (which is linear in t)

$$\widehat{B}_{\rm t}[\Delta,J]_q=2(\Delta-J+2q+1-\tfrac{\rm t}{2})\frac{(\frac{\Delta-J-2}{2})^2_q}{(-J-4)_q}-4\frac{(\frac{\Delta-J-2}{2})^2_{q+1}}{(-J-4)_{q+1}}, \tag{C.15}$$

which we dot into the Mack coefficients:

$$\widehat{B}_{\rm t}[\Delta,J]=\tilde{K}^{N=4}_{\Delta,J}\sum_{q,k=0}^{J}\widehat{B}_{\rm t}[\Delta,J]_q\left[Q^{0,0}_{\Delta+4,J}\right]_{q,k}\frac{(\frac{\rm t-2}{2})_k}{\rm t-6}. \tag{C.16}$$

The result takes the form of a polynomial in t of degree $J+1$, divided by $({\rm t}-6)$. At this stage we typically express it as a Pochhammer sum,

$$\widehat{B}_{\rm t}[\Delta,J]\equiv\tilde{K}^{N=4}_{\Delta,J}\sum_{k=0}^{J+1}B[\Delta,J]_k\frac{(\frac{\rm t-2}{2})_k}{\rm t-6} \tag{C.17}$$

where the coefficients $B[\Delta,J]_k$ can be obtained from the above using simple vector operations.

This representation is useful to compute various functionals related to B. For example, the Mellin transform which gives the position functional B_v (3.13) can be done analytically using

$$\frac{1}{2}\int\frac{d{\rm t}}{4\pi i}v^{\frac{\rm t}{2}-4}\Gamma\big(4-\tfrac{\rm t}{2}\big)^2\Gamma\big(\tfrac{\rm t}{2}-1\big)^2\frac{(\frac{\rm t-2}{2})_k}{\rm t-6}=\frac{-\Gamma(k+3)}{2(k+2)_3}{}_2F_1(3,k+3,k+5,1-v)\equiv[B_v]_k\,, \tag{C.18}$$

which allows to compute the position space functional as $B_v[\Delta,J]=\tilde{K}^{N=4}_{\Delta,J}\sum_k B[\Delta,J]_k\,[B_v]_k$.

The results (and performance) can be compared with the position space integrals described in section C.1. For a sample operator with $J=150$ and twist $4+\frac{1}{19}$, and $v=3/2$, we find for example:

$$\begin{aligned}B_{3/2}[150,154+\tfrac{1}{19}]&=2.845137906\ldots\times10^{83}&&\text{(position, 4s)}\\&=2.8451379417996980420\ldots\times10^{83}&&\text{(position, 20s)}\\&=2.8451379417996980643304973 1\ldots\times10^{83}&&\text{(Mellin, 1s)}\end{aligned} \tag{C.19}$$

The accurate agreement between methods is a crucial debugging tool which gives us high confidence in our implementation. The Mellin space version of B functionals is clearly faster, especially when high accuracy is needed. This is partly due to the sub-exponential convergence of the ρ integrations discussed above. In contrast, the Mellin formula boils down to the exact calculation of a matrix of rational numbers, times a numerical vector of ${}_2F_1$ functions, whose cost increases very slowly with the requested precision.

The projection functionals $\Phi_{\ell,\ell'}$ and Ψ_ℓ are computed similarly using respectively the vectors (B.37) and (B.42), so that

$$\Phi_{\ell,\ell'}[\Delta,J] = \tilde{K}^{N=4}_{\Delta,J}\sum_{k=0}^{J+1} B[\Delta,J]_k \left[\Phi_{\ell,\ell'}\right]_k, \quad \Psi_\ell[\Delta,J] = \tilde{K}^{N=4}_{\Delta,J}\sum_{k=0}^{J+1} B[\Delta,J]_k \left[\Psi_\ell\right]_k. \tag{C.20}$$

Note that the vectors of rational numbers $[\Phi_{\ell,\ell+2}]_k$ and $[\Psi_\ell]_k$ only need be computed once. The projection functionals are thus obtained to infinite accuracy in effectively no time, after the $B[\Delta,J]_k$ coefficients have been calculated once.

C.4 Formulas for Polyakov-Regge blocks using Mack polynomials

A similar strategy works for the Mellin-space Polyakov-Regge block (3.8), whose definition we recall:

$$\widehat{\mathcal{P}}^{N=4}_{\mathrm{s,t}}[\Delta,J] = \sum_{m=0}^{\infty} \mathcal{Q}^{m,\{4,4,4,4\}}_{\Delta+4,J}(16-\mathrm{s}-\mathrm{t})\left[\frac{1}{\mathrm{s}-(\Delta-J+2m+4)}+\frac{1}{\mathrm{t}-(\Delta-J+2m+4)}\right]. \tag{C.21}$$

The effect of the denominator is to replace the vector of m-sums (C.15) by

$$\widehat{\mathcal{P}}^{N=4}_{\mathrm{s}}[\Delta,J]_q \equiv \sum_{m=0}^{\infty} \frac{K^{m,\{\Delta_i\}}_{\Delta,J}}{\tilde{K}^{N=4}_{\Delta,J}} \frac{(-m)_q}{\mathrm{s}-(\Delta-J+2m+4)}. \tag{C.22}$$

It turns out that this sum can also be evaluated analytically, now in terms of ${}_3F_2$ hypergeometric functions. Explicitly, for $q=0$ we find:

$$\widehat{\mathcal{P}}^{N=4}[\Delta,J]_{\mathrm{s},0} = \frac{\Gamma\left(\frac{\Delta+J}{2}+4\right)^2}{\Gamma(\Delta+3)\Gamma(J+5)} \frac{{}_3F_2\left(\left\{\frac{\Delta-J-2}{2},\frac{\Delta-J-2}{2},\frac{\Delta-J-\mathrm{s}}{2}+2\right\},\left\{\frac{\Delta-J-\mathrm{s}}{2}+3,\Delta+3\right\},1\right)}{\mathrm{s}-(\Delta-J+4)}. \tag{C.23}$$

The terms with $q>0$ admit similar expressions, but a more efficient strategy is to compute them recursively, using combinations that cancel out the m-dependent denominator:

$$\widehat{\mathcal{P}}^{N=4}[\Delta,J]_{\mathrm{s},q+1} = (q+\tfrac{\Delta-J+4-\mathrm{s}}{2})\widehat{\mathcal{P}}^{N=4}[\Delta,J]_{\mathrm{s},q} + \frac{(\frac{\Delta-J-2}{2})^2_q}{2(-J-4)_q}. \tag{C.24}$$

The inhomogeneous term equals the sum of $K^{m,\{\Delta_i\}}_{\Delta,J}(-m)_q/(2\tilde{K}^{N=4}_{\Delta,J})$, computed using (C.13). Once the vector (C.22) is populated, eqs. (C.6) and (C.21) readily give the following formula

for Polyakov-Regge blocks:

$$\widehat{\mathcal{P}}^{N=4}_{\mathrm{s,t}}[\Delta,J]=\tilde{K}^{N=4}_{\Delta,J}\sum_{q,k=0}^{J}\left(\widehat{\mathcal{P}}^{N=4}_{\mathrm{s}}[\Delta,J]_q+\widehat{\mathcal{P}}^{N=4}_{\mathrm{t}}[\Delta,J]_q\right)\left[Q^{0,0}_{\Delta+4,J}\right]_{q,k}\left(\tfrac{\mathrm{s+t-8}}{2}\right)_k. \tag{C.25}$$

Again this can be rapidly calculated to very high accuracy.

The above expression is also well-suited for performing the Mellin transform to obtain the position-space blocks $\mathcal{P}_{u,v}$. For the term with $\mathcal{P}_{\mathrm{s}}$, the Mellin integral over t can be done analytically and gives (with $\mathrm{u}=16-\mathrm{s}-\mathrm{t}$):

$$\begin{aligned}\Gamma\left(\tfrac{\mathrm{s}}{2}\right)^{-2}\int\frac{d\mathrm{t}}{4\pi i}v^{\frac{\mathrm{t}}{2}-4}\Gamma\left(4-\tfrac{\mathrm{t}}{2}\right)^2\Gamma\left(\tfrac{\mathrm{s+t-8}}{2}\right)^2\left(\tfrac{\mathrm{s+t-8}}{2}\right)_k&=\frac{\Gamma\left(k+\frac{\mathrm{s}}{2}\right)^2}{\Gamma(k+\mathrm{s})}{}_2F_1\left(\tfrac{\mathrm{s}}{2},\tfrac{\mathrm{s}}{2}+k,\mathrm{s}+k,1-v\right)\\&\equiv[\mathcal{P}_{\mathrm{s},v}]_k\,.\end{aligned} \tag{C.26}$$

A rapid way to compute this vector is described below. The outcome is $\mathcal{P}_{\Delta,J}(u,v)$ written as a single integral over a matrix product:[10]

$$\frac{\mathcal{P}_{\Delta,J}(u,v)}{\tilde{K}^{N=4}_{\Delta,J}}=\int\frac{d\mathrm{s}}{4\pi i}\Gamma\left(\tfrac{\mathrm{s}}{2}\right)^2\Gamma\left(4-\tfrac{\mathrm{s}}{2}\right)^2\sum_{q,k=0}^{J}\widehat{\mathcal{P}}^{N=4}_{\mathrm{s}}[\Delta,J]_q\left[Q^{0,0}_{\Delta+4,J}\right]_{q,k}\left(u^{\frac{\mathrm{s}}{2}-4}[\mathcal{P}_{\mathrm{s},v}]_k+v^{\frac{\mathrm{s}}{2}-4}[\mathcal{P}_{\mathrm{s},u}]_k\right). \tag{C.27}$$

There is a single integral left to perform numerically, over s, in contrast with the two-dimensional ρ integral in the position-space approach. However, the integrand is a fairly complicated function of s, especially at large spin J.

Fortunately, it turns out that the s integral in (C.27) is "nice" for numerics. We use an exponential parametrization $\mathrm{s}=5+i\sinh(x)$ and simply approximate the integral by a Riemann sum, sampling x at discrete values uniformly spaced in a range such as $[-6,6]$. Since the integrand decays doubly exponentially with x, it is easy to ascertain that the contribution from x outside the range is smaller than say 10^{-200}. Furthermore, since the function is smooth, the Euler-Maclaurin theorem predicts that discretization errors decay nonpertubatively with the spacing Δx. We observe empirically that the error decays as $e^{-\#/\Delta x}$ with $\#\sim 4$ for a wide range of spins, twists, and cross-ratios.

Convergence is extremely fast. The Riemann sum using just 300 sampling points is typically accurate to 50 digits. Thus, our method for evaluating $\mathcal{P}_{\Delta,J}(u,v)$ boils down to evaluating the vectors $\widehat{\mathcal{P}}^{N=4}_{\mathrm{s}}[\Delta,J]_q$ and $[\mathcal{P}_{\mathrm{s},u/v}]_k$ on a few hundreds values of s, and dotting into the Mack coefficient matrix $\left[Q^{0,0}_{\Delta+4,J}\right]_{q,k}$. The result is highly accurate and stable under changes in the parametrization or in the real part of s.

This method agrees precisely with the position space integrals described above. Again, it is instructive to compare the results (and performance on one of the authors' laptop) of

[10] The factorization of the q and v dependence of the integrand is related to the fact that we study unsubtracted dispersion relation.

the two methods:

$$\begin{aligned} X_{2/3,5/4}[150, 154 + \tfrac{1}{19}] &= 1.947607331\ldots \times 10^{78} (\text{position, } 30\text{s}) \\ &= 1.947607348863473773952667853129889 6\ldots \times 10^{78} (\text{position, } 1800\text{s}) \\ &= 1.9476073\ldots \times 10^{78} (\text{Mellin, } 700\text{s}) \\ &= 1.947607348863473773952667853129889 6365\ldots \times 10^{78} (\text{Mellin, } 1200\text{s}). \end{aligned} \tag{C.28}$$

Again, the precise agreement gives us high confidence in the validity of our codes. Generally, our position space implementation tends to be faster for getting a small number of figures, but its cost increases rapidly with the requested accuracy. On the other hand, the Mellin method requires some effort to get any significant figure at all (due to strong numerical cancellations in the matrix product), but it scales much better with requested accuracy. The above timings reflects a naive implementation of the ${}_3F_2$ function (C.23), which is the most expensive step in the calculation; faster timings are achieved using the optimizations below.

A significant advantage of the Mellin approach is that the same ingredients can be recycled for many functionals. This makes the average evaluation time per functional much smaller than the above numbers suggest. Most of our intensive runs were computed using this method.

C.5 Some algorithmic improvements

For the reasons just mentioned, we invested significant effort to optimize Mellin-based formulas. The most expensive ingredient in the preceding subsection is to perform the sum over descendants in (C.22) for $q = 0$, which we expand here for convenience:

$$\widehat{\mathcal{P}}_{\text{s}}^{N=4}[\Delta, J]_0 \equiv \frac{\Gamma\left(\frac{\Delta+J}{2}+4\right)^2}{\Gamma(\Delta+3)\Gamma(J+5)} \sum_{m=0}^{\infty} \frac{\left(\frac{\Delta-J-2}{2}\right)_m^2}{(\Delta+3)_m m!} \frac{1}{\text{s} - (\Delta - J + 2m + 4)}. \tag{C.29}$$

We focus here on the sum which appears in $\mathcal{N} = 4$ sYM, but we expect similar techniques to work for the more general dispersive sum rules discussed in [41]. A relevant fact is that for each (Δ, J), we need the above sum for several hundred values of s. Instead of using `Mathematica`'s `HypergeometricPFQ`, we find it advantageous to compute the sum by combining exact evaluation of the summand at small m with its asymptotic series at large m:

$$\widehat{\mathcal{P}}_{\text{s}}^{N=4}[\Delta, J]_0 = \sum_{m=0}^{m_{\max}} \frac{X_m}{\text{s} - (\Delta - J + 2m + 4)} + \sum_{m_{\max}+1}^{\infty} \left[\sum_{n=0}^{n_{\max}} \frac{Y_n}{m^{J+6+n}} \frac{1}{\text{s} - (\Delta - J + 2m + 4)}\right], \tag{C.30}$$

where X_m collects all other factors in (C.29) and the Y_n parametrize its $1/m$ expansion. In the last term, the m-sum can be rapidly computed as a series in $1/m_{\max}$ up to order $n_{\max}$. For calculations aiming for $O(100)$ digits, we typically choose $n_{\max} \sim 100$ or more, and increase it and $m_{\max}$ until the error in the formula becomes smaller than the requested precision. Errors are readily estimated using the observation that the X_m sum up to exactly 1 (see (C.13)).

The crucial point is that the expensive ingredients in this formula, X_m and Y_n, only need to be evaluated once for each operator (Δ, J): the s-dependent factor is very simple. The sum

can thus be computed for multiple s values for essentially the price of one, easily reducing the timings quoted in (C.28) by two orders of magnitude.

The second expensive ingredient is the vector of ${}_2F_1$ functions in (C.26). We evaluate it by replacing it by linear combinations that involve ρ-like variables and computing those recursively. Specifically, define the two-vector:

$$\mathcal{P}'_{\mathrm{s},v} \equiv \frac{\Gamma\left(\frac{\mathrm{s}}{2}\right)^2}{\Gamma(\mathrm{s})}(1+\rho_v)^{\mathrm{s}} \begin{pmatrix} {}_2F_1\left(\frac{1}{2},\frac{\mathrm{s}}{2},\frac{\mathrm{s}+1}{2},\rho_v^2\right) \\ {}_2F_1\left(\frac{3}{2},\frac{\mathrm{s}}{2},\frac{\mathrm{s}+3}{2},\rho_v^2\right) \end{pmatrix}, \qquad \rho_v \equiv \frac{1-\sqrt{v}}{1+\sqrt{v}}. \tag{C.31}$$

The desired integral (C.26) can be expressed in terms of those using

$$\Gamma\left(\tfrac{\mathrm{s}}{2}\right)^{-2} \int \frac{d\mathrm{t}}{4\pi i} v^{\frac{\mathrm{t}}{2}-4} \Gamma\left(4-\tfrac{\mathrm{t}}{2}\right)^2 \Gamma\left(\tfrac{\mathrm{s}+\mathrm{t}-8}{2}\right)^2 \begin{pmatrix} \left(\frac{\mathrm{s}+\mathrm{t}-8}{2}\right)_r^2 \\ \left(\frac{\mathrm{s}+\mathrm{t}-8}{2}\right)_r \left(\frac{\mathrm{s}+\mathrm{t}-8}{2}\right)_{r+1} \end{pmatrix} \tag{C.32}$$

$$= \left(\tfrac{\mathrm{s}}{2}\right)_r^2 \begin{pmatrix} 1 & 0 \\ \frac{1+\rho_v}{4}(\mathrm{s}+2r) - \frac{\rho_v}{4} & \frac{\rho_v}{4} \end{pmatrix} \cdot \mathcal{P}'_{\mathrm{s}+2r,v}\,. \tag{C.33}$$

More precisely, the integral $[\mathcal{P}_{\mathrm{s},v}]_k$ is equal to a sum of the left-hand-side of the preceding equation with $0 \le r \le \lfloor \frac{k}{2} \rfloor$ and integer coefficients. The two-vectors $\mathcal{P}'_{\mathrm{s}+2r,v}$ which appear on the right-hand-side can be populated recursively in terms of the one with the largest r, using

$$\mathcal{P}'_{\mathrm{s},v} = \frac{4}{\mathrm{s}(1+\rho_v)^2} \begin{pmatrix} \mathrm{s}+1 & -\rho_v^2 \\ 1 & (\mathrm{s}-1)\rho_v^2 \end{pmatrix} \cdot \mathcal{P}'_{\mathrm{s}+2,v}\,. \tag{C.34}$$

(We avoid using the recursion in the opposite direction because it is not numerically stable for $v \approx 1$.) Even without the change of basis (C.33), hypergeometric relations would allow the vector $[\mathcal{P}_{\mathrm{s},v}]_k$ to be populated with only two hypergeometric evaluations, a significant speedup over $O(J)$ evaluations. The special combinations (C.31) further optimize the computation of two seeds by making the hypergeometric argument numerically smaller (see [69]).

References

[1] N. Beisert et al., *Review of AdS/CFT Integrability: An Overview*, *Lett. Math. Phys.* **99** (2012) 3–32, [1012.3982].

[2] B. Basso, A. Sever and P. Vieira, *Spacetime and Flux Tube S-Matrices at Finite Coupling for N=4 Supersymmetric Yang-Mills Theory*, *Phys. Rev. Lett.* **111** (2013) 091602, [1303.1396].

[3] A. Sever, A. G. Tumanov and M. Wilhelm, *Operator Product Expansion for Form Factors*, *Phys. Rev. Lett.* **126** (2021) 031602, [2009.11297].

[4] L. J. Dixon, O. Gurdogan, A. J. McLeod and M. Wilhelm, *Bootstrapping a Stress-Tensor Form Factor through Eight Loops*, 2204.11901.

[5] S. Caron-Huot, L. J. Dixon, F. Dulat, M. von Hippel, A. J. McLeod and G. Papathanasiou, *Six-Gluon amplitudes in planar $\mathcal{N}$ = 4 super-Yang-Mills theory at six and seven loops*, *JHEP* **08** (2019) 016, [1903.10890].

[6] L. J. Dixon and Y.-T. Liu, *Lifting Heptagon Symbols to Functions*, *JHEP* **10** (2020) 031, [2007.12966].

[7] D. J. Binder, S. M. Chester, S. S. Pufu and Y. Wang, $\mathcal{N} = 4$ *Super-Yang-Mills correlators at strong coupling from string theory and localization*, *JHEP* **12** (2019) 119, [1902.06263].

[8] S. M. Chester, R. Dempsey and S. S. Pufu, *Bootstrapping* $\mathcal{N} = 4$ *super-Yang-Mills on the conformal manifold*, 2111.07989.

[9] M. S. Costa, V. Goncalves and J. Penedones, *Conformal Regge theory*, *JHEP* **12** (2012) 091, [1209.4355].

[10] V. Gonçalves, *Four point function of* $\mathcal{N} = 4$ *stress-tensor multiplet at strong coupling*, *JHEP* **04** (2015) 150, [1411.1675].

[11] L. F. Alday, A. Bissi and E. Perlmutter, *Genus-One String Amplitudes from Conformal Field Theory*, *JHEP* **06** (2019) 010, [1809.10670].

[12] Z. Huang and E. Y. Yuan, *Graviton Scattering in* $\mathrm{AdS}_5 \times \mathrm{S}^5$ *at Two Loops*, 2112.15174.

[13] J. M. Drummond and H. Paul, *Two-loop supergravity on* $AdS_5 \times S^5$ *from CFT*, 2204.01829.

[14] V. Gonçalves, R. Pereira and X. Zhou, 20′ *Five-Point Function from* $AdS_5 \times S^5$ *Supergravity*, *JHEP* **10** (2019) 247, [1906.05305].

[15] N. Gromov, V. Kazakov and P. Vieira, *Exact Spectrum of Anomalous Dimensions of Planar N=4 Supersymmetric Yang-Mills Theory*, *Phys. Rev. Lett.* **103** (2009) 131601, [0901.3753].

[16] N. Gromov, V. Kazakov, S. Leurent and D. Volin, *Quantum Spectral Curve for Planar* $\mathcal{N} = 4$ *Super-Yang-Mills Theory*, *Phys. Rev. Lett.* **112** (2014) 011602, [1305.1939].

[17] N. Gromov, V. Kazakov, S. Leurent and D. Volin, *Quantum spectral curve for arbitrary state/operator in* AdS_5/CFT_4, *JHEP* **09** (2015) 187, [1405.4857].

[18] N. Gromov, *Introduction to the Spectrum of* $N = 4$ *SYM and the Quantum Spectral Curve*, 1708.03648.

[19] B. Basso, S. Komatsu and P. Vieira, *Structure Constants and Integrable Bootstrap in Planar N=4 SYM Theory*, 1505.06745.

[20] T. Fleury and S. Komatsu, *Hexagonalization of Correlation Functions*, *JHEP* **01** (2017) 130, [1611.05577].

[21] F. Coronado, *Perturbative four-point functions in planar* $\mathcal{N} = 4$ *SYM from hexagonalization*, *JHEP* **01** (2019) 056, [1811.00467].

[22] F. Coronado, *Bootstrapping the Simplest Correlator in Planar* $\mathcal{N} = 4$ *Supersymmetric Yang-Mills Theory to All Loops*, *Phys. Rev. Lett.* **124** (2020) 171601, [1811.03282].

[23] T. Bargheer, F. Coronado and P. Vieira, *Octagons I: Combinatorics and Non-Planar Resummations*, *JHEP* **08** (2019) 162, [1904.00965].

[24] T. Bargheer, F. Coronado and P. Vieira, *Octagons II: Strong Coupling*, 1909.04077.

[25] R. Rattazzi, V. S. Rychkov, E. Tonni and A. Vichi, *Bounding scalar operator dimensions in 4D CFT*, *JHEP* **12** (2008) 031, [0807.0004].

[26] S. El-Showk, M. F. Paulos, D. Poland, S. Rychkov, D. Simmons-Duffin and A. Vichi, *Solving the 3D Ising Model with the Conformal Bootstrap*, *Phys. Rev. D* **86** (2012) 025022, [1203.6064].

[27] D. Poland, S. Rychkov and A. Vichi, *The Conformal Bootstrap: Theory, Numerical Techniques, and Applications*, *Rev. Mod. Phys.* **91** (2019) 015002, [1805.04405].

[28] D. Poland and D. Simmons-Duffin, *Snowmass White Paper: The Numerical Conformal Bootstrap*, in *2022 Snowmass Summer Study*, 3, 2022, 2203.08117.

[29] C. Beem, L. Rastelli and B. C. van Rees, *More $\mathcal{N} = 4$ superconformal bootstrap*, *Phys. Rev. D* **96** (2017) 046014, [1612.02363].

[30] A. Cavaglià, N. Gromov, J. Julius and M. Preti, *Integrability and conformal bootstrap: One dimensional defect conformal field theory*, *Phys. Rev. D* **105** (2022) L021902, [2107.08510].

[31] A. Cavaglià, N. Gromov, J. Julius and M. Preti, *Bootstrability in defect CFT: integrated correlators and sharper bounds*, *JHEP* **05** (2022) 164, [2203.09556].

[32] B. Eden, C. Jarczak and E. Sokatchev, *A Three-loop test of the dilatation operator in N = 4 SYM*, *Nucl. Phys. B* **712** (2005) 157–195, [hep-th/0409009].

[33] B. C. Vallilo and L. Mazzucato, *The Konishi multiplet at strong coupling*, *JHEP* **12** (2011) 029, [1102.1219].

[34] N. Gromov, F. Levkovich-Maslyuk and G. Sizov, *Quantum Spectral Curve and the Numerical Solution of the Spectral Problem in AdS5/CFT4*, *JHEP* **06** (2016) 036, [1504.06640].

[35] A. Hegedús and J. Konczer, *Strong coupling results in the AdS_5 /CF T_4 correspondence from the numerical solution of the quantum spectral curve*, *JHEP* **08** (2016) 061, [1604.02346].

[36] A. Georgoudis, V. Goncalves and R. Pereira, *Konishi OPE coefficient at the five loop order*, *JHEP* **11** (2018) 184, [1710.06419].

[37] J. A. Minahan and R. Pereira, *Three-point correlators from string amplitudes: Mixing and Regge spins*, *JHEP* **04** (2015) 134, [1410.4746].

[38] J. Penedones, J. A. Silva and A. Zhiboedov, *Nonperturbative Mellin Amplitudes: Existence, Properties, Applications*, *JHEP* **08** (2020) 031, [1912.11100].

[39] S. Caron-Huot, D. Mazac, L. Rastelli and D. Simmons-Duffin, *Dispersive CFT Sum Rules*, *JHEP* **05** (2021) 243, [2008.04931].

[40] S. Caron-Huot, D. Mazac, L. Rastelli and D. Simmons-Duffin, *AdS bulk locality from sharp CFT bounds*, *JHEP* **11** (2021) 164, [2106.10274].

[41] A.-K. Trinh, *Mixed correlator dispersive CFT sum rules*, *JHEP* **03** (2022) 032, [2111.14731].

[42] D. Carmi and S. Caron-Huot, *A Conformal Dispersion Relation: Correlations from Absorption*, *JHEP* **09** (2020) 009, [1910.12123].

[43] F. A. Dolan, L. Gallot and E. Sokatchev, *On four-point functions of 1/2-BPS operators in general dimensions*, *JHEP* **09** (2004) 056, [hep-th/0405180].

[44] M. Nirschl and H. Osborn, *Superconformal Ward identities and their solution*, *Nucl. Phys. B* **711** (2005) 409–479, [hep-th/0407060].

[45] F. A. Dolan and H. Osborn, *Conformal partial wave expansions for N=4 chiral four point functions*, *Annals Phys.* **321** (2006) 581–626, [hep-th/0412335].

[46] G. Arutyunov, F. A. Dolan, H. Osborn and E. Sokatchev, *Correlation functions and massive Kaluza-Klein modes in the AdS / CFT correspondence*, *Nucl. Phys. B* **665** (2003) 273–324, [hep-th/0212116].

[47] S. Caron-Huot, *Analyticity in Spin in Conformal Theories*, *JHEP* **09** (2017) 078, [1703.00278].

[48] C. Marboe and D. Volin, *The full spectrum of AdS_5/CFT_4 II: Weak coupling expansion via the quantum spectral curve*, *J. Phys. A* **54** (2021) 055201, [1812.09238].

[49] J. Drummond, C. Duhr, B. Eden, P. Heslop, J. Pennington and V. A. Smirnov, *Leading singularities and off-shell conformal integrals*, *JHEP* **08** (2013) 133, [1303.6909].

[50] L. Freyhult and S. Zieme, *The virtual scaling function of AdS/CFT*, *Phys. Rev. D* **79** (2009) 105009, [0901.2749].

[51] B. Basso and G. P. Korchemsky, *Anomalous dimensions of high-spin operators beyond the leading order*, *Nucl. Phys. B* **775** (2007) 1–30, [hep-th/0612247].

[52] L. F. Alday, A. Bissi and T. Lukowski, *Large spin systematics in CFT*, *JHEP* **11** (2015) 101, [1502.07707].

[53] N. Gromov, F. Levkovich-Maslyuk, G. Sizov and S. Valatka, *Quantum spectral curve at work: from small spin to strong coupling in $\mathcal{N} = 4$ SYM*, *JHEP* **07** (2014) 156, [1402.0871].

[54] L. F. Alday, T. Hansen and J. A. Silva, *AdS Virasoro-Shapiro from dispersive sum rules*, 2204.07542.

[55] A. V. Kotikov, L. N. Lipatov and V. N. Velizhanin, *Anomalous dimensions of Wilson operators in N=4 SYM theory*, *Phys. Lett. B* **557** (2003) 114–120, [hep-ph/0301021].

[56] A. V. Kotikov, L. N. Lipatov, A. I. Onishchenko and V. N. Velizhanin, *Three loop universal anomalous dimension of the Wilson operators in $N = 4$ SUSY Yang-Mills model*, *Phys. Lett. B* **595** (2004) 521–529, [hep-th/0404092].

[57] B. Eden, *Three-loop universal structure constants in N=4 susy Yang-Mills theory*, 1207.3112.

[58] J. Henriksson and T. Lukowski, *Perturbative Four-Point Functions from the Analytic Conformal Bootstrap*, *JHEP* **02** (2018) 123, [1710.06242].

[59] D. Simmons-Duffin, *A Semidefinite Program Solver for the Conformal Bootstrap*, *JHEP* **06** (2015) 174, [1502.02033].

[60] F. Kos, D. Poland and D. Simmons-Duffin, *Bootstrapping Mixed Correlators in the 3D Ising Model*, *JHEP* **11** (2014) 109, [1406.4858].

[61] D. Poland, D. Simmons-Duffin and A. Vichi, *Carving Out the Space of 4D CFTs*, *JHEP* **05** (2012) 110, [1109.5176].

[62] S. M. Chester and S. S. Pufu, *Far beyond the planar limit in strongly-coupled $\mathcal{N} = 4$ SYM*, *JHEP* **01** (2021) 103, [2003.08412].

[63] B. Basso, *Exciting the GKP string at any coupling*, *Nucl. Phys. B* **857** (2012) 254–334, [1010.5237].

[64] B. Basso, A. Sever and P. Vieira, *Space-time S-matrix and Flux tube S-matrix II. Extracting and Matching Data*, *JHEP* **01** (2014) 008, [1306.2058].

[65] N. Beisert, B. Eden and M. Staudacher, *Transcendentality and Crossing*, *J. Stat. Mech.* **0701** (2007) P01021, [hep-th/0610251].

[66] N. Beisert, *The Dilatation operator of N=4 super Yang-Mills theory and integrability*, *Phys. Rept.* **405** (2004) 1–202, [hep-th/0407277].

[67] S. Komatsu, *Three-point functions in $\mathcal{N} = 4$ supersymmetric Yang–Mills theory*, 1710.03853.

[68] B. Eden and A. Sfondrini, *Tessellating cushions: four-point functions in $\mathcal{N} = 4$ SYM*, *JHEP* **10** (2017) 098, [1611.05436].

[69] M. Hogervorst and S. Rychkov, *Radial Coordinates for Conformal Blocks*, *Phys. Rev. D* **87** (2013) 106004, [1303.1111].

[70] G. Mack, *D-independent representation of Conformal Field Theories in D dimensions via transformation to auxiliary Dual Resonance Models. Scalar amplitudes*, 0907.2407.